CM² MAGAZINE

第 81 期

南方科技大学海洋磁学中心主编

http://cm2.sustech.edu.cn/

创刊词

海洋是生命的摇篮，是文明的纽带。地球上最早的生命诞生于海洋，海洋里的生命最终进化成了人类，人类的文化融合又通过海洋得以实现。人因海而兴。

人类对海洋的探索从未停止。从远古时代美丽的神话传说，到麦哲伦的全球航行，再到现代对大洋的科学钻探计划，海洋逐渐从人类敬畏崇拜幻想的精神寄托演变成可以开发利用与科学研究的客观存在。其中，上个世纪与太空探索同步发展的大洋科学钻探计划将人类对海洋的认知推向了崭新的纬度：深海（deep sea）与深时（deep time）。大洋钻探计划让人类知道，奔流不息的大海之下，埋藏的却是亿万年的地球历史。它们记录了地球板块的运动，从而使板块构造学说得到证实；它们记录了地球环境的演变，从而让古海洋学方兴未艾。

在探索海洋的悠久历史中，从大航海时代的导航，到大洋钻探计划中不可或缺的磁性地层学，磁学发挥了不可替代的作用。这不是偶然，因为从微观到宏观，磁性是最基本的物理属性之一，可以说，万物皆有磁性。基于课题组的学科背景和对海洋的理解，我们对海洋的探索以磁学为主要手段，海洋磁学中心因此而生。

海洋磁学中心，简称 CM^2，一为其全名“Centre for Marine Magnetism”的缩写，另者恰与爱因斯坦著名的质能方程 $E = MC^2$ 对称，借以表达我们对科学巨匠的敬仰和对科学的不懈追求。

然而科学从来不是单打独斗的产物。我们以磁学为研究海洋的主攻利器，但绝不仅限于磁学。凡与磁学相关的领域均是我们关注的重点。为了跟踪反映国内外地球科学特别是与磁学有关的地球科学领域的最新研究进展，海洋磁学中心特地主办 CM^2 Magazine，以期与各位地球科学工作者相互交流学习、合作共进！

“海洋孕育了生命，联通了世界，促进了发展”。 21 世纪是海洋科学的时代，由陆向海，让我们携手迈进中国海洋科学的黄金时代。

目录

1. 末次冰期-间冰期旋回内北格林兰冰心的铁与亚洲粉尘记录相关

翻译人：仲义 zhongy@sustech.edu.cn

Xiao C, Du Z, Handley M J, et al. ***Iron in the NEEM ice core relative to Asian loess records over the last glacial-interglacial cycle*** *[J] National Science Review, 8(7), nwaa 144. https://doi.org/10.1093/nsr/nwaa144.*

摘要：矿物性粉尘能够间接地通过提供可利用铁（Fe）进入海洋来改变全球气候变化。本文中作者展示了过去 110 千年以来北格林兰冰心中溶解铁（DFe）和总铁（TDFe）的记录。冷期时铁含量与 CO_2 变化呈现明显的负相关。结果说明过去 100 千年铁通量与中国黄土记录呈现一致性变化，因为矿物性粉尘分布受到东亚沙漠的控制。进而，全球范围内粉尘输入的变化很可能是由于太阳辐射的变化驱动的，在最后一个冰期旋回内响应于地球轨道周期变化。在末次冰期-间冰期旋回内，暖期（后工业革命之后、全新世和末次间冰期）DFe/TDFe 比值相对于主要的冷期（末次盛冰期）更高，显示出风尘输入的铁与铁肥效应对海洋的作用在不同时期呈现非线性关系。虽然自工业革命以来生物质气溶胶的燃烧释放了大量的溶解铁，但是在这一时期 DFe 和 TDFe 的变化没有显著响应，表明严重的人类污染对 NEEM 冰心中 DFe（TDFe）的释放没有产生重要影响。

ABSTRACT: Mineral dust can indirectly affect the climate by supplying bioavailable iron (Fe) to the ocean. Here, we present the records of dissolved Fe (DFe) and total Fe (TDFe) in North Greenland Eemian Ice Drilling (NEEM) ice core over the past 110 kyr BP. The Fe records are significantly negatively correlated with the carbon-dioxide (CO_2) concentrations during cold periods. The results suggest that the changes in Fe fluxes over the past 110 kyr BP in the NEEM ice core are consistent with those in Chinese loess records because the mineral-dust distribution is controlled by the East Asian deserts. Furthermore, the variations in the dust input on a global scale are most likely driven by changes in solar radiation during the last glacial–interglacial cycle in response to Earth's orbital cycles. In the last glacial–interglacial cycle, the DFe/TDFe ratios were higher during the warm periods (following the post-Industrial Revolution and during the Holocene and last interglacial period) than during the main cold period (i.e. the last glacial maximum (LGM)), indicating that the aeolian input of iron and the iron

fertilization effect on the oceans have a non-linear relationship during different periods. Although the burning of biomass aerosols has released large amounts of DFe since the Industrial Revolution, no significant responses are observed in the DFe and TDFe variations during this period, indicating that severe anthropogenic contamination has no significant effect on the DFe (TDFe) release in the NEEM ice core.

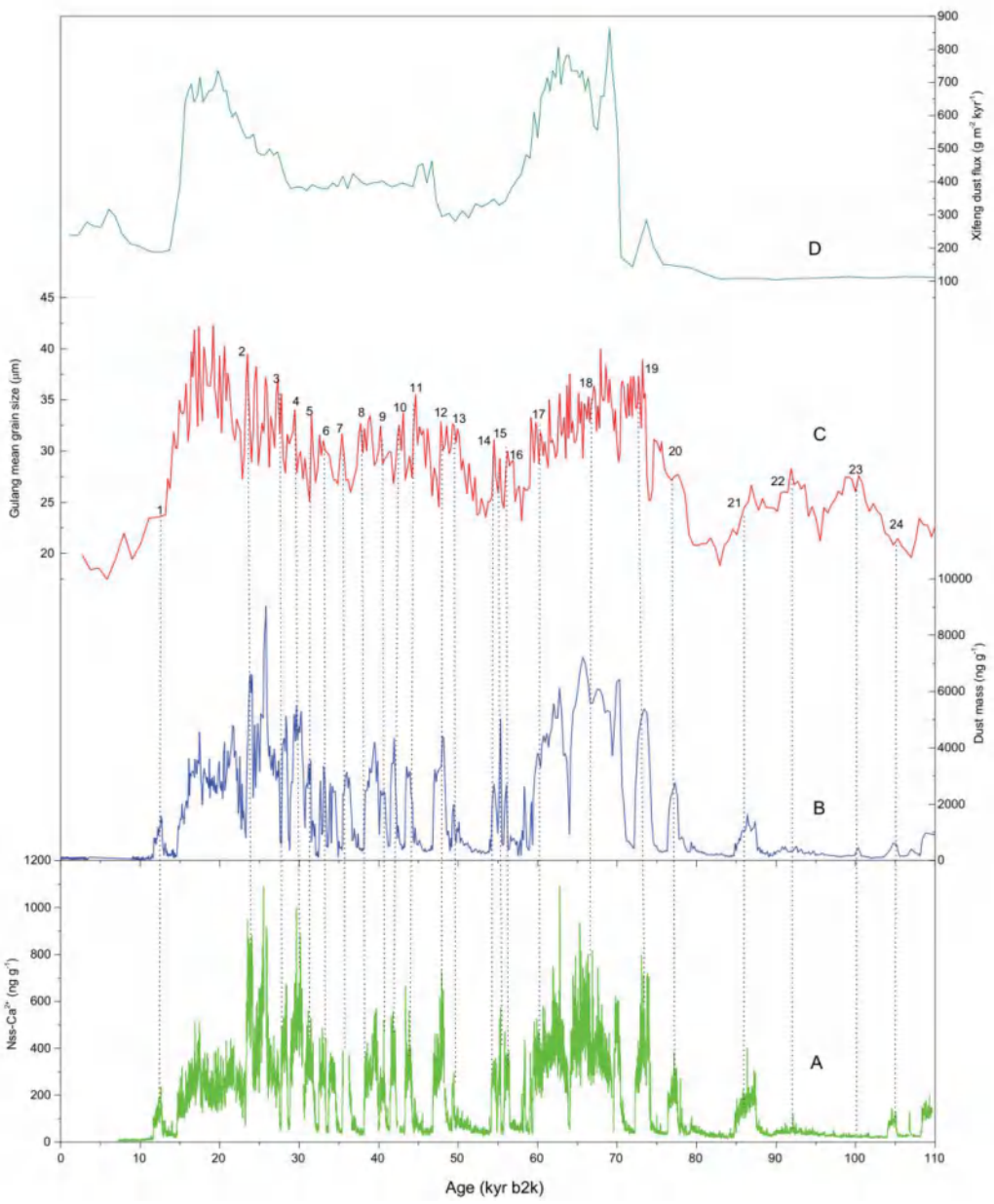

Figure 1. Comparison of the concentrations of Nss-Ca^{2+} (A), the dust mass (B) in the NEEM ice core from this study, the median grain size in the Gulang record (C and the Xifeng dust fluxes (D). The dotted lines show the correlation of 24 D-O cycles between the NEEM ice core and the Gulang loess.

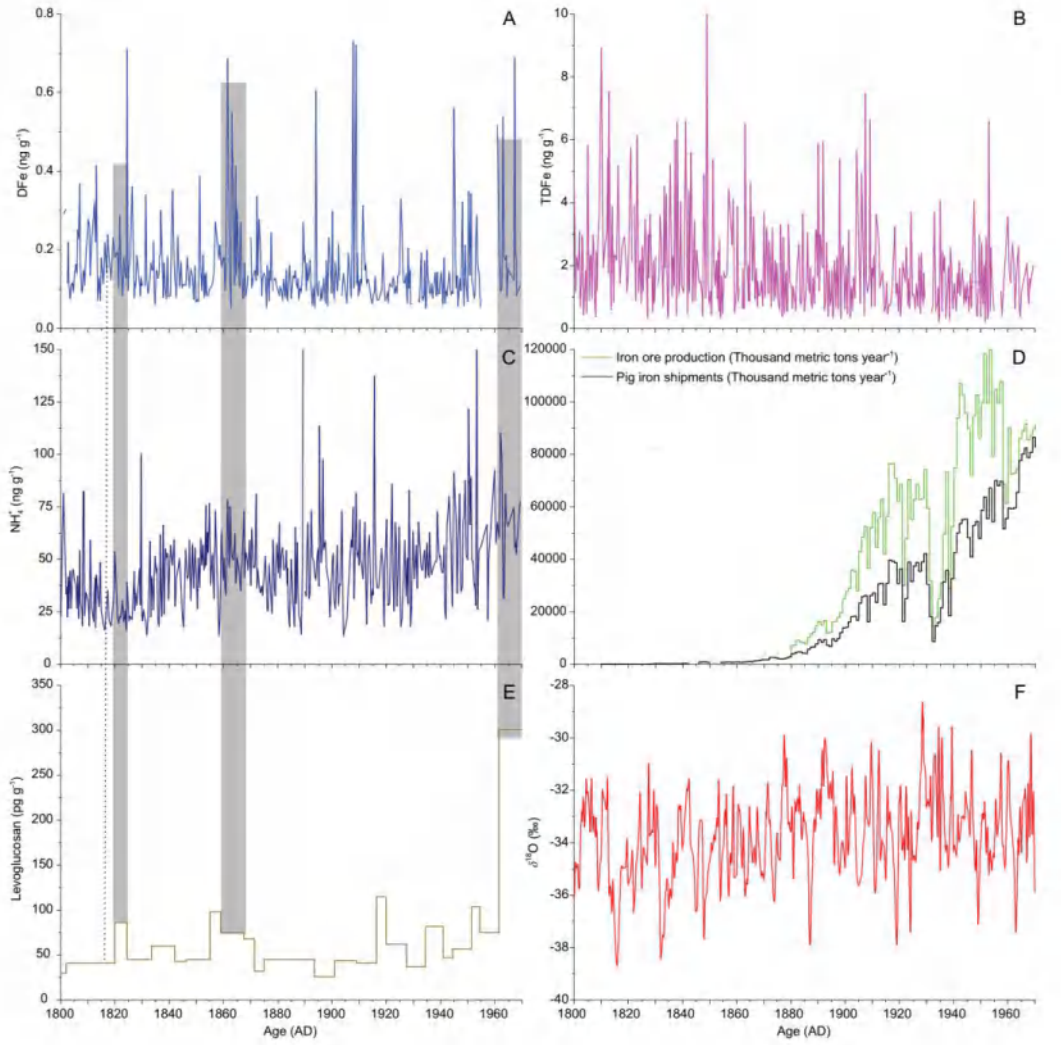

Figure 2. DFe, TDFe and NH^{4+} concentrations (A–C) and $\delta^{18}O$ values in the NEEM 2009 shallow Core 1 (F), the levoglucosan concentration in NEEM 2011 S1 (E) and the iron-ore production and pig-iron shipments data (D) from the USA between 1800 and 1970. The dashed line in parts (A, C and E) represents the Tambora eruption in 1815. Gray shadings represent the peaks between DFe and NH^{4+} and levoglucosan concentrations.

2. 火山灰的海洋成岩作用助于古新世-始新世极热事件（PETM）终止

翻译人：蒋晓东 jiangxd@sustech.edu.cn

Longmana J, Gernonc M T, Palmerc M R, et al. ***Marine diagenesis of tephra aided the Palaeocene-Eocene Thermal Maximum termination*** *[J]. Earth and Planetary Science Letters, 2021. 571, 117101.*

https://doi.org/10.1016/j.epsl.2021.117101

摘要：古新世-始新世极热（PETM）是一个约发生在 55.9 Ma，持续时间约为 170 ky 的全球急速变暖的事件。包括北大西洋火山岩省在内的多个机制被认为是引起这次事件的触发因素。同样地，被认为封存二氧化碳的多种机制也被提出，该机制使全球温度恢复到温和的条件。本文基于火山灰胶结物中碳酸钙沉积的研究，提出一种重要的关于北大西洋火山岩省的碳封存机制。我们发现 PETM 期间这些胶结物在北大西洋火山岩省覆盖区广泛出现，并形成于火山灰埋藏之后。另有强有力的证据表明这些自生碳酸钙胶结物是在火山灰埋藏后短时间内形成。蒙特卡洛模拟表明这一过程可能在 PETM 恢复阶段封存了四分之一碳量。这一发现提供了先前未考虑的机制，也是同位素轻碳封存的主要过程，并且这一过程持续到了始新世时期。

ABSTRACT: The Palaeocene-Eocene Thermal Maximum (PETM) was a period of intense global warming that began ~55.9 million years ago and lasted about 170,000yrs. Various mechanisms have been proposed to cause this warming, including the emplacement of the North Atlantic Igneous Province (NAIP). Equally, many mechanisms have been invoked to explain sequestration of carbon from the ocean-atmosphere system necessary to promote the recovery to more temperate conditions. Here we propose that an important path for carbon sequestration was tied to NAIP volcanism through the precipitation of calcium carbonate ($CaCO_3$) cements within the tephra layers. These cements formed after the deposition and burial of tephra over a wide area of the North Atlantic Ocean during the late Palaeocene and early Eocene. We find strong evidence that authigenic $CaCO_3$ cements formed shortly after tephra deposition. Monte Carlo simulations suggest that this process may have been responsible for a quarter of the carbon sequestered during the PETM recovery phase,

providing a major, but previously unconsidered sink of isotopically-light carbon, and one which may have persisted into the Eocene.

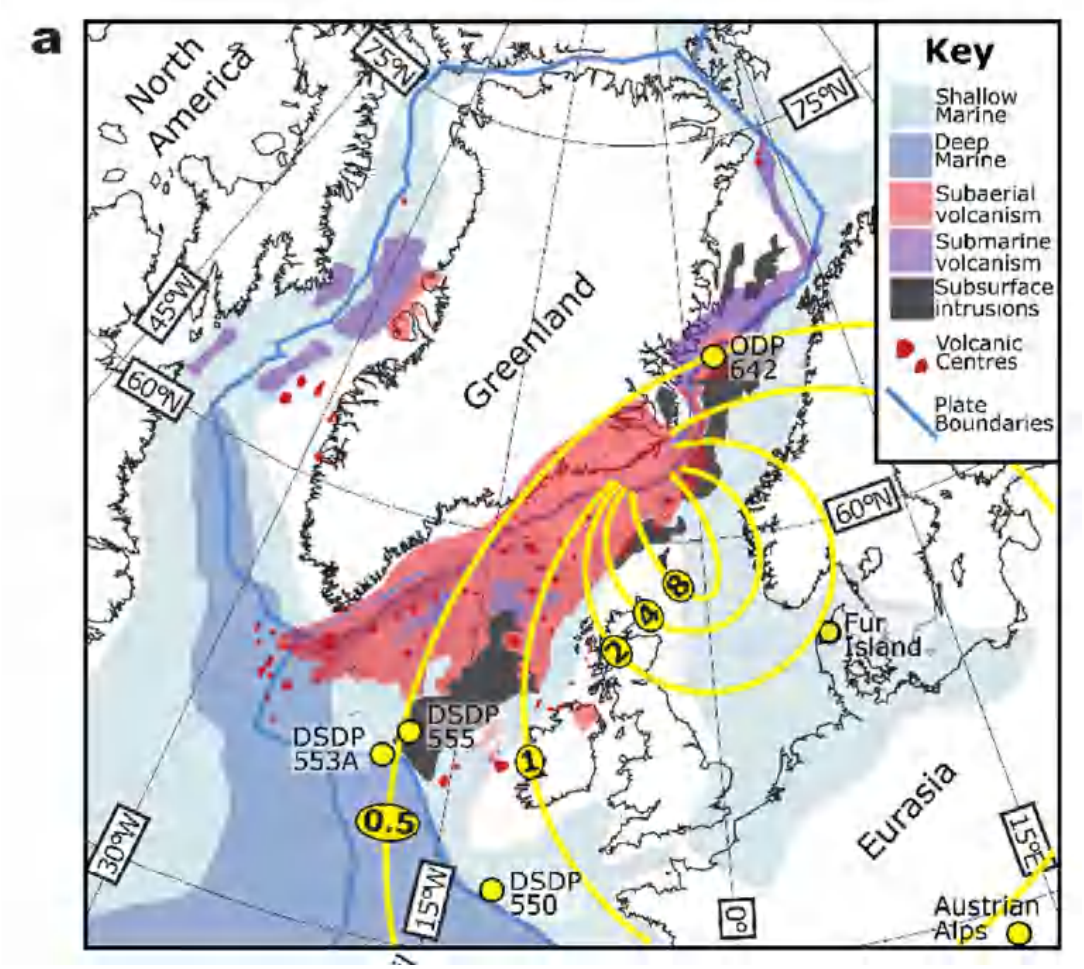

Figure 1. Spatial and temporal distribution of tephras analysed in this study. (a) Palaeo-geographic reconstruction of the North Atlantic region at circa 55 Ma displaying an overview of the North Atlantic Igneous Province (NAIP), adapted from Jones et al. (2019). Locations of shallow and deep marine basins are represented by light and dark blue areas, respectively. Locations of extrusive (subaerial and submarine) vol-canism are marked in red, with dark red designating discrete volcanic centres. Areas of sill intrusions into sedimentary basins are shown in dark brown. Note that seis-mic retrievals below volcanic extrusives are very poor, so the extent of intrusions may be considerable below the red areas shown on the map. Also shown, in yel-low, are isopachs of levels of tephra fall (in metres) from explosive volcanism during the period of NAIP activity (taken from Obst et al. (2015)). Locations mentioned in this study are labelled with yellow circles.

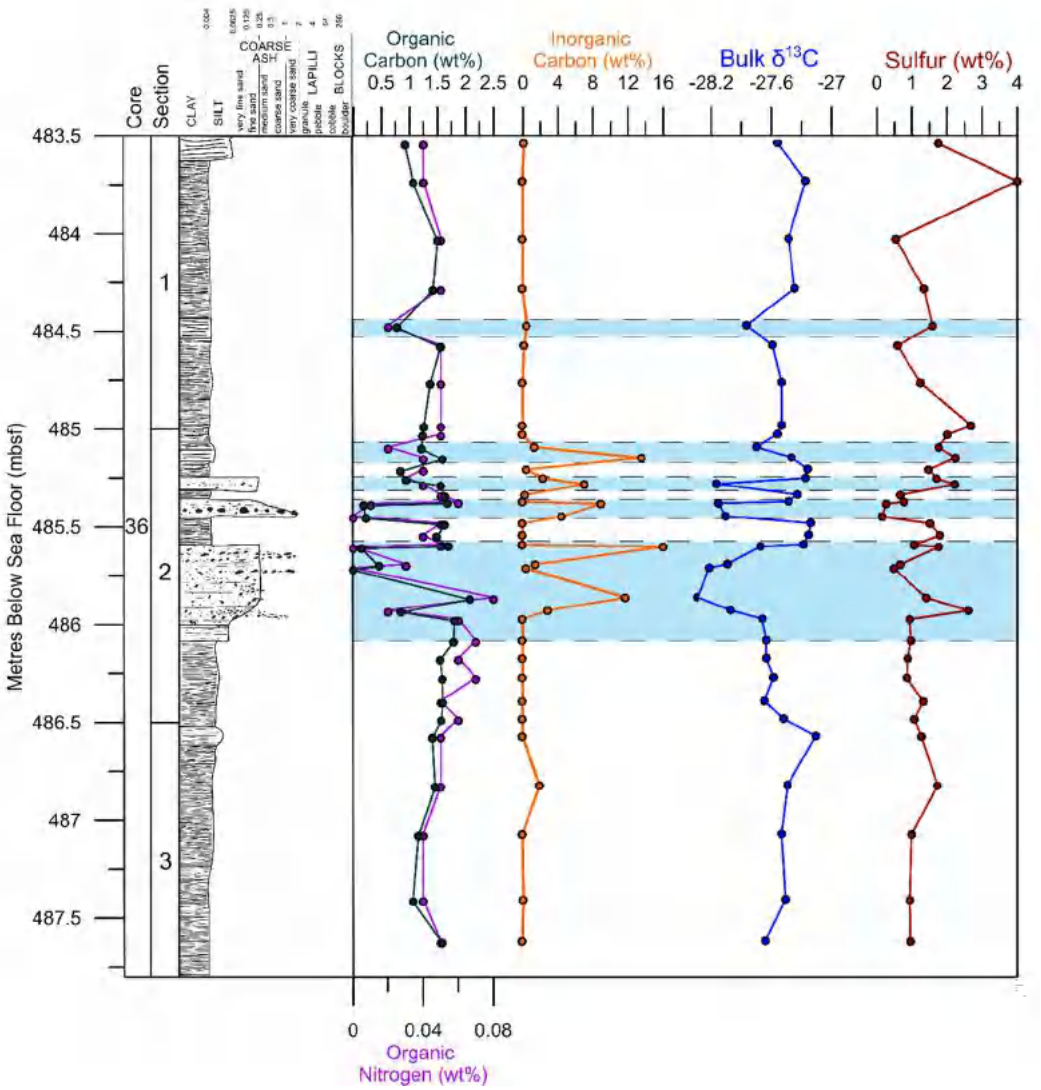

Figure 2. Carbon and sulfur characteristics of tephras and sediments in Hole 553A (Rockall). The downhole graphs show organic carbon, inorganic carbon, organic nitrogen, and sulfur concentrations (in wt%). Also shown is the bulk $\delta^{13}C$ signal, relative to VPDB, and a simplified graphic log of the mudrock and tephra sequence. Tephra layers are highlighted in blue and are consistently enriched in $CaCO_3$ and depleted in organic carbon and $\delta^{13}C$, demonstrating the regular occurrence of carbonate minerals within these layers.

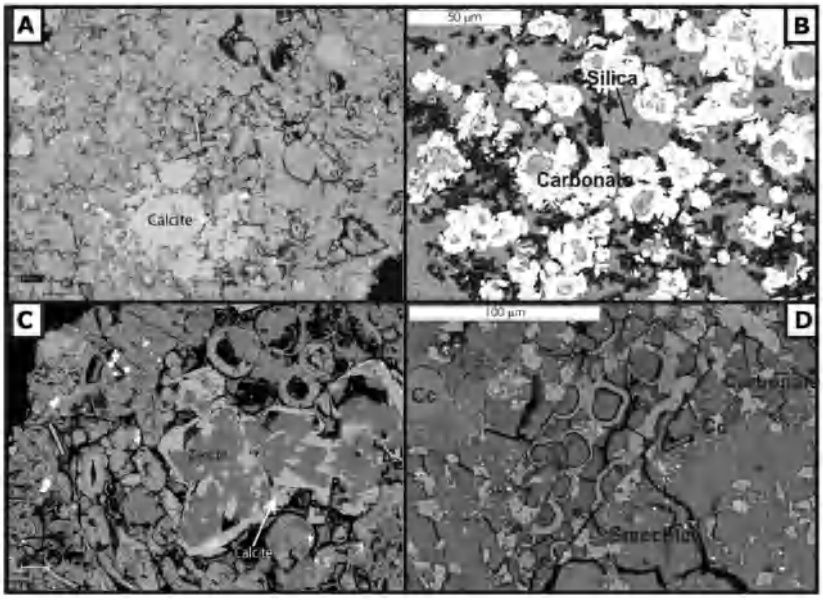

Figure 3. SEM images of authigenic carbonate formation in ash layers. Panels A and C shows tephras from the Rockall sequences, A is from ash layer present in DSDP Hole 553A (Core 36, Section2, 69-71cm). B is from ash layer present in DSDP Hole 555 (Core 65, Section1, 105-107cm). Panels B and D shows carbonate infilling as calcite (cc) in samples from core 6607/12-1 from the Vøring Basin.

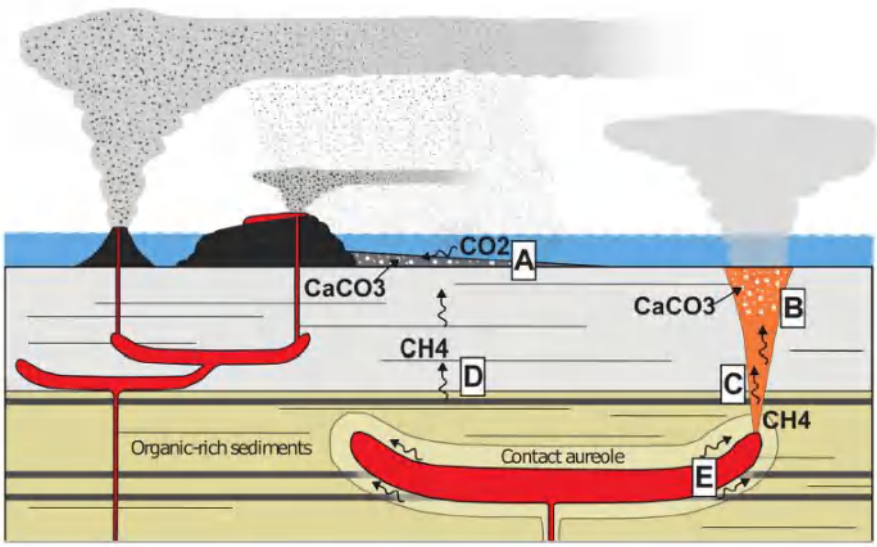

Figure 4. Schematic diagram (not to scale) showing the locations of carbonate formation, and pathways of carbon migration during the PETM. The locations of authigenic carbonate cement formation are (a) in tephra layers and (b) above hydrothermal vent structures. To form these carbonate cements, carbon may be sourced from (c) methane release during hydrothermal vent activity, (d) methane tied to anaerobic oxidation of organic sediments, and (e) methane degassing from contact metamorphism when sills are emplaced in organic-rich sediments. Figure is modified after Heimdal et al. (2019); Jones et al. (2019).

3. 阿富汗碳酸盐岩火山揭示俯冲沉积碳的快速循环

翻译人：冯婉仪 fengwy@sustech.edu.cn

Horton F. ***Rapid recycling of subducted sedimentary carbon revealed by Afghanistan carbonatite volcano*** *[J]. Nature Geoscience, 2021, online.*

https://doi.org/10.1038/s41561-021-00764-7

摘要：碳俯冲到地幔深处的命运仍不确定，但强烈地影响着地质时间尺度上陆地碳的分布。进入俯冲带的碳通量在含有厚的沉积扇的俯冲板块处异常的高。本研究利用火山地球化学来评估高通量 Makran 俯冲带的沉积碳循环，在那里阿拉伯板块向北俯冲至欧亚大陆之下。根据锶同位素地球化学和 ^{40}Ar-^{39}Ar 地质年代学，我发现一部分海底印度河扇进入 Makran 海沟，熔融、上升为岩浆，并在阿富汗南部喷发。由此形成的火山，主要由碳酸盐矿物组成，形成于大约 3.8 Ma 之前。熔岩的 $^{87}Sr/^{86}Sr$ 比值表明其母岩浆来源于 28.9 ± 1.4 Ma 的海洋沉积物。这意味着沉积碳在不到 27 Ma 的时间里俯冲到地幔深处并从地幔深处折返，这表明岩浆可以有效地将俯冲板片的沉积碳循环到上覆板块。

ABSTRACT: The fate of carbon subducted to mantle depths remains uncertain, yet strongly influences the distribution of terrestrial carbon on geologic timescales. Carbon fluxes into subduction zones are exceptionally high where downgoing plates contain thick sedimentary fans. This study uses volcano geochemistry to assess sedimentary carbon recycling in the high-flux Makran subduction zone, where the Arabian plate subducts northward beneath Eurasia. On the basis of strontium isotope geochemistry and ^{40}Ar–^{39}Ar geochronology, I show that a portion of the submarine Indus Fan entered the Makran Trench, melted and ascended as magmas that erupted in southern Afghanistan. The resulting volcano, composed primarily of carbonate minerals, formed at approximately 3.8 million years ago. The $^{87}Sr/^{86}Sr$ ratios of the lavas indicate that their magmatic precursors were derived from marine sediments deposited at 28.9 ± 1.4 Ma. This implies that sedimentary carbon was subducted to and returned from mantle depths in less than 27 million years, indicating that magmas can efficiently recycle sedimentary carbon from subducting slabs to the overlying plate.

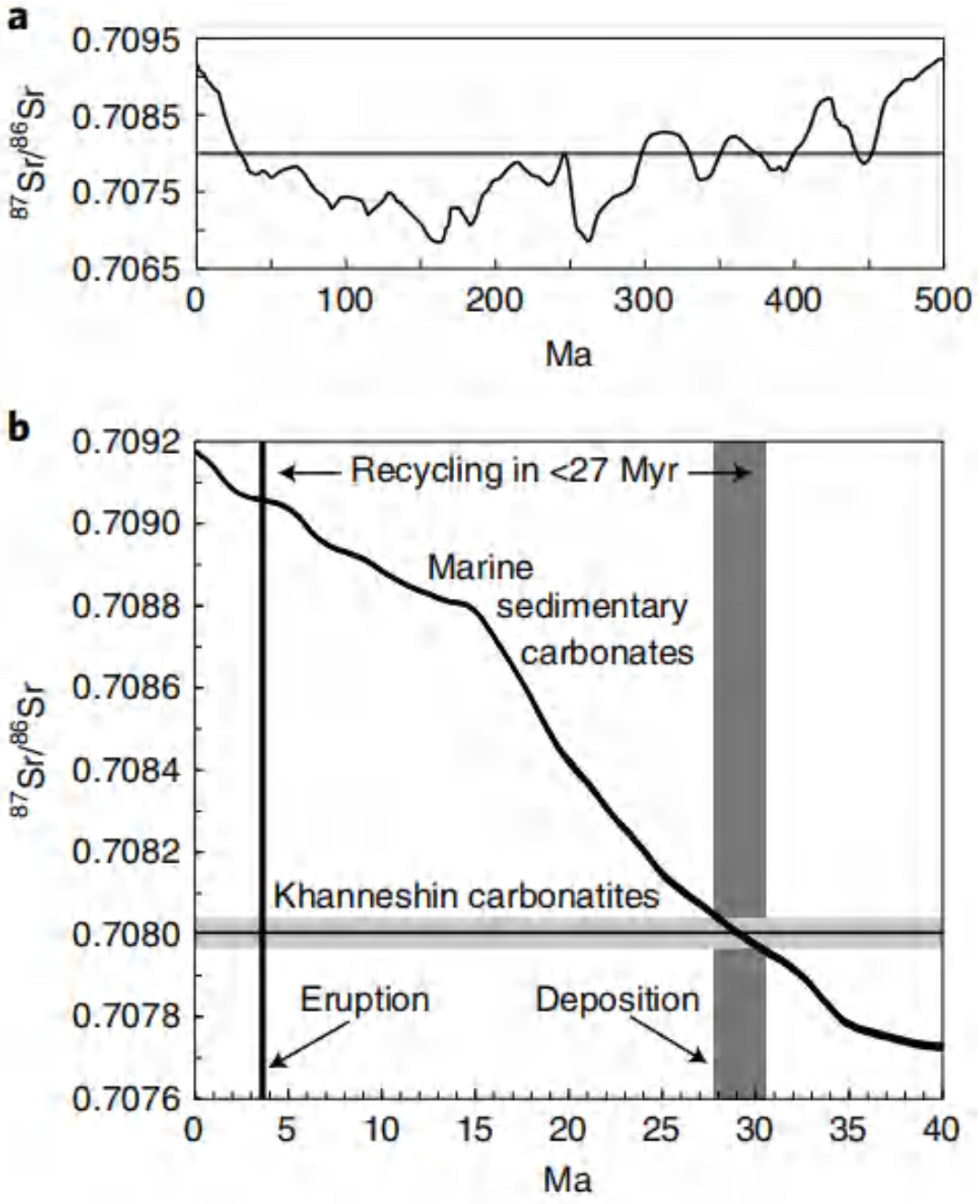

Figure 1. Strontium isotopic evidence of rapid sediment recycling. a, The $^{87}Sr/^{86}Sr$ of Khanneshin carbonatites versus average marine sedimentary carbonates[41]. The horizontal black line and the bounding light grey area represent the mean (n= 20 rocks) and ± 1 s.d., respectively, for the Khanneshin carbonatites. Since 500 Ma, average marine sedimentary carbonate compositions have equalled that measured in the Khanneshin carbonatites nine times, but only once since 200 Ma. b, As in a, but from 0 to 40 Ma. Sediments deposited in the Indus Fan at circa 30 Ma would have had $^{87}Sr/^{86}Sr$ ratios comparable to those measured in the Khanneshin samples. This implies that sediment recycling through the Makran subduction zone took less than 27 Myr.

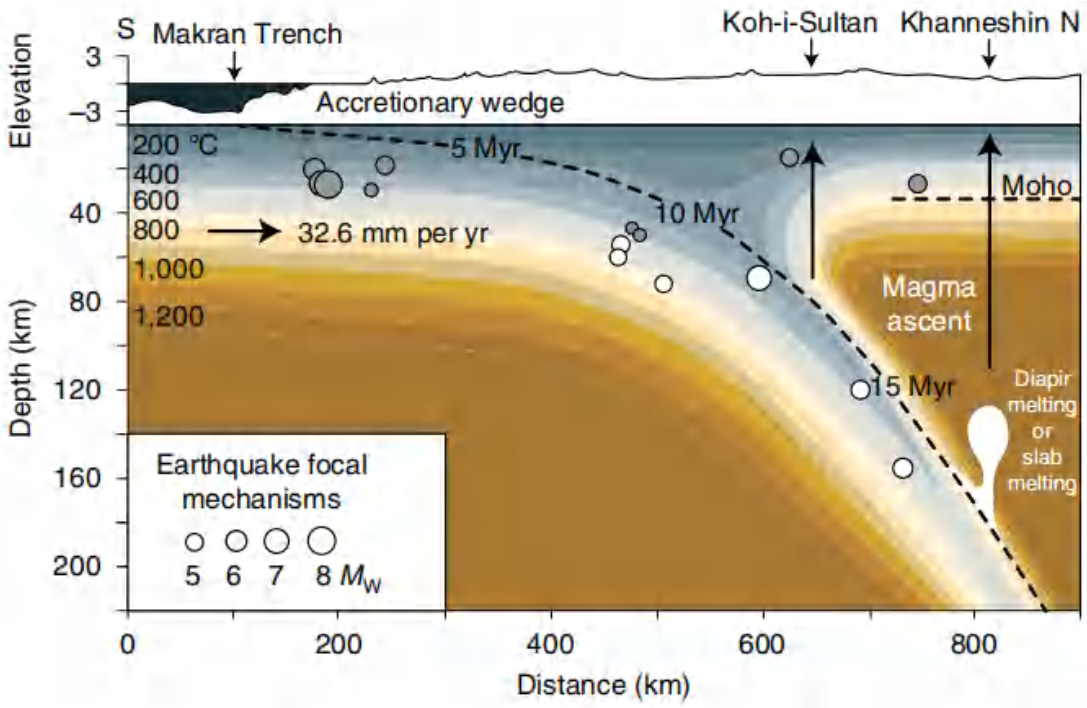

Figure 2. Schematic cross-section of the eastern Makran subduction zone. Khanneshin magmas are probably derived from subducted sediments that melted near the top of the subducting slab or in buoyant diapirs that ascended into the mantle wedge. Slab depths and the thermal structure are based on earthquake focal mechanisms[17] and thermal modelling[30], respectively. The black dashed line along the top of the subducting Arabian plate represents the trajectory of subducted Indus Fan material and the time elapsed since entering the trench. Earthquakes with focal mechanisms < 50 km deep are shown as grey circles.

4. 水星幔对流的停止能否允许发电机支撑其核热损失的增加？

翻译人:李园洁 liyj3@sustech.edu.cn

Guerrero J M, Lowman J P, Tackley P J. ***Did the cessation of convection in Mercury's mantle allow for a dynamo supporting increase in heat loss from its core? [J]****. Earth and Planetary Science Letters, 2021, 571: 117108.*

https://doi.org/10.1016/j.epsl.2021.117108

摘要:水星的核产生磁场并具有一个固态的内核。这些特征可为星球的热历史模型提供约束。水星幔能确定热损失提供水核的边界条件。最近的研究表明由于铁亏损水幔比其他星球的硅酸盐壳具有更高的热扩散率。考虑到扩散率的作用，我们构建水星幔从后岩浆海状态开始，计算与太阳系年龄相当的时期内核幔边界热损失和内核边界半径与核幔边界半径之比 f_c。核幔边界热损失的计算是利用 3D 幔对流模拟，假定热扩散率 κ，范围为 1.0-3.0 $\times 10^{-6} m^2/s$，初始辐射成因均匀幔的升温速率 χ 为 0 - 40 pW/kg （3Gyr 半衰期）。对于可考虑的参数范围，可展开几种情况：这些包含幔对流停止和 4.5 Gyr 时继续的两种情况的特征。我们绘制了的趋势，发现对于一些参数现在的核热流和内核尺寸的估计可以满足水星幔通过传导降温。估计了水核内的初始硫分馏的影响。对于 0.10 的硫分馏，f_c 将降低到 0.1-0.55，相当于行星半径收缩在 7 km 以下（自后期重轰炸期）。然而，更低的硫分馏，f_c 超过 0.55 导致行星收缩超过 7 公里。总之，我们发现当水幔从对流过渡到传导时平均核热流达到暂时的局部极小值之后上升然后下降。随着水幔内部加热速率的增加，向传导的过渡被延迟，但是从水核到传导的冷却的水幔的热流平均最大值总是高于滞盖对流停止观测到的热流。我们发现对于最初对流更强烈的幔，内核开始生长得更早，而热流目前略微降低。总之，我们发现了目前水星幔的传导冷却能够满足从磁场强度推断的水核热损失，同时满足其内核现今尺寸的限制。

ABSTRACT： Mercury's large core generates a magnetic field and harbors a solidified inner component. These features constrain models of the planet's thermal history. The mantle provides the boundary condition on Mercury's core that determines heat loss. Recent studies suggest Mercury's mantle may have a higher thermal diffusivity than the silicate shells of other rocky bodies

due to iron depletion. Considering the role of diffusivity, we model Mercury's mantle starting from a post magma-ocean state by calculating core-mantle boundary heat flow and the ratio of inner-core boundary radius to core-mantle boundary radius, f_c, for periods comparable to the age of the solar system. Core-mantle boundary (CMB) heat flow is calculated using 3D mantle convection simulations for thermal diffusivities, κ, ranging from 1.0-3.0 $\times 10^{-6} m^2/s$ and initial radiogenic uniform mantle heating rates, χ, of 0 - 40 pW/kg (that decay with a 3 Gyr half-life). Several scenarios can unfold for the range of parameters considered: these include cases featuring both the cessation of mantle convection and its continuation at 4.5 Gyr. We map a trend in κ - χ space and find that for some parameters present-day core heat flux and inner-core size estimates are satisfied for a Mercurian mantle that is cooling by conduction. The influence of initial sulfur fraction in the core was examined for a subset of cases. For a sulfur fraction of 0.10, f_c falls between 0.1 and 0.55 which corresponds to planetary radius contractions below 7 km (since the Late Heavy Bombardment). However, f_c exceeds 0.55 for a lower initial sulfur fraction and results in planetary contraction in excess of 7 km. In general, we find that the mean core heat flux reaches a temporal local minimum when the mantle transitions from a convective to a conductive regime and subsequently climbs before decreasing. The transition to conduction is delayed with increased mantle internal heating rate but the maximum mean heat flux from the core into the conducting and cooling mantle is always greater than the heat flux observed at the cessation of the stagnant-lid convection. We find that for an initially more vigorously convecting mantle the onset of inner-core growth is earlier while the basal heat flux is marginally reduced at present day. In general, we find that current-day conductive cooling of the Mercurian mantle can satisfy estimates on Mercury's core heat loss inferred from the strength of its magnetic field while also satisfying the limits on the present-day size of its inner core.

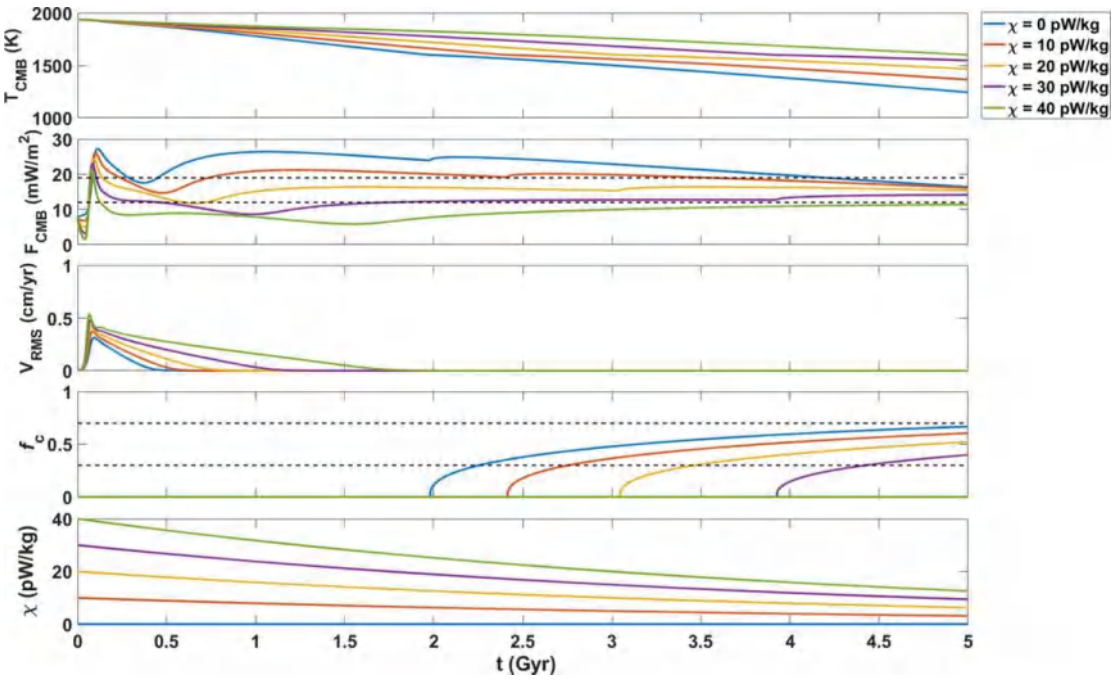

Figure 1. Timeseries are plotted for the mean CMB temperature (first panel), mean basal heat flux (second panel), V_{RMS} (third panel), ratio of the inner-core boundary radius to core-mantle boundary radius (f_c) (fourth panel), and mantle internal heating rate (fifth panel) for five calculations with different initial internal heat production rates (indicated in the legend) and $\kappa = 2.0 \times 10^{-6}$ m^2/s. In the second panel, a range of core heat flux values (12 - 19 mW/m^2) is indicated by the dashed black lines. In the fourth panel, a range of f_c values (0.3 - 0.7) is indicated by the dashed black lines. (The interpretation of the colors in the figures can be referred to in the web version of the article.).

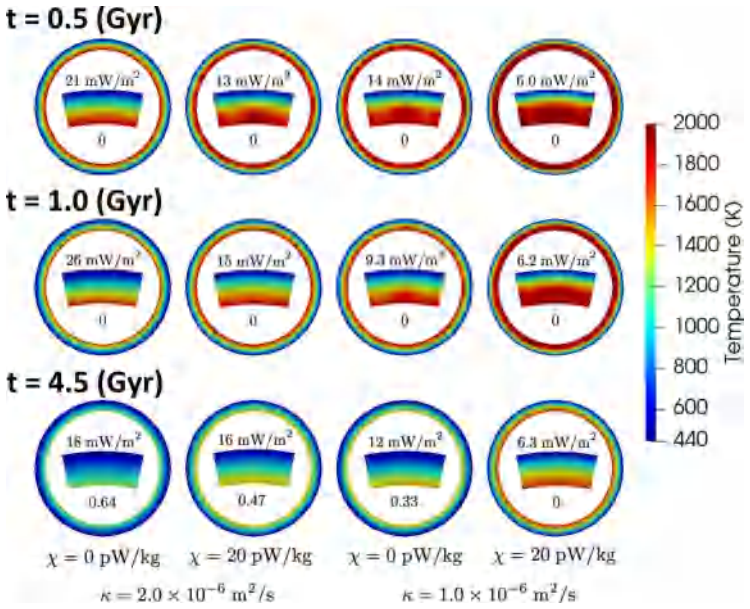

Figure 2. Temperature field slices at 0.5, 1.0, and 4.5 Gyr for cases featuring $\kappa = 2.0 \times 10^{-6}$ m^2/s (first and second columns) and $\kappa = 1.0 \times 10^{-6}$ m^2/s (third and fourth columns). Calculations for two different initial internal heating rates are presented. There is no internal heating in the first and third columns and χ= 20 pW/kg in the second and fourth columns. A segment of the spherical shell from the north pole of each 360° slice is shown by an inset and the corresponding basal heat flux value in mW/m^2 as well as the inner-core boundary to core-mantle boundary radius ratio is inscribed within the slice. Time is indicated on the left in Gyr and super-adiabatic temperature, in Kelvins, is indicated on the colorbar.

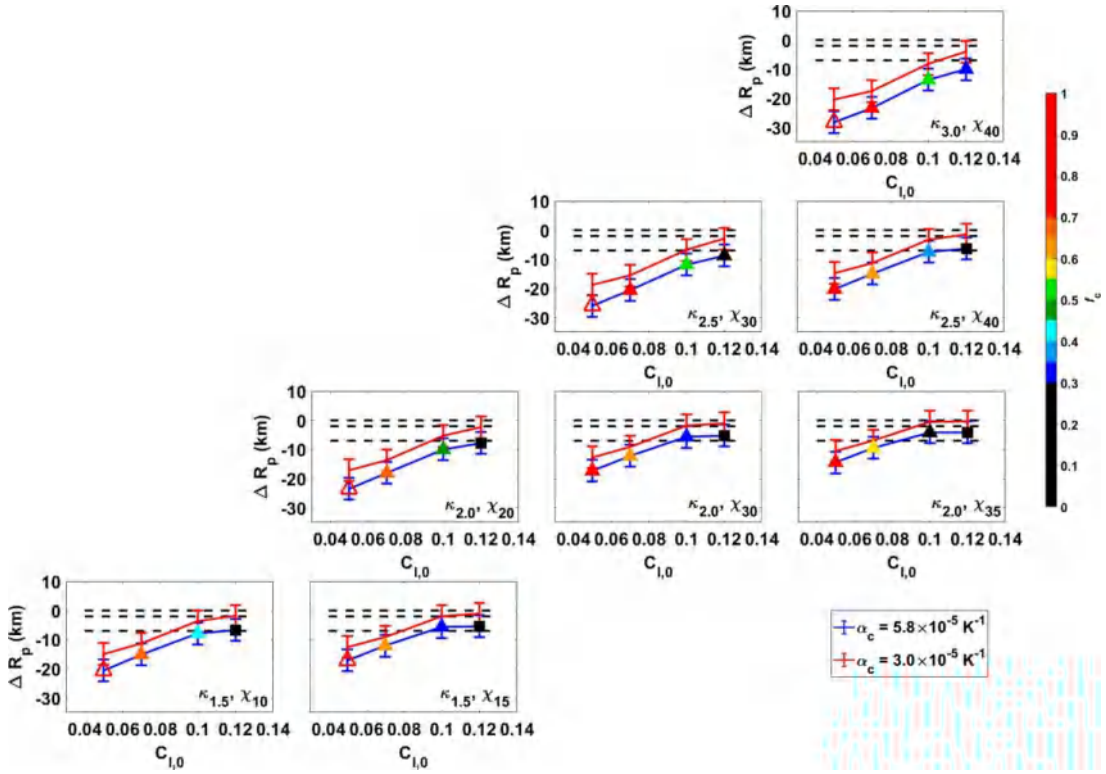

Figure 3. Planetary radius contraction at 4.5 Gyr is plotted as a function of the initial fraction of sulfur in the core for select cases with $\kappa = 1.5, 2.0, 2.5$ and 3.0×10^{-6} m^2/s. The κ and χ values are indicated in the bottom right of each panel and are arranged similarly to the green-blue band. The blue curve indicates the planetary radial contraction assuming a core thermal expansivity, αc, of 5.8×10^{-5} K^{-1} and the red curve indicates radial contraction assuming $\alpha_c = 3.0 \times 10^{-5}$ K^{-1}. For each case plotted, the upper and lower bounds correspond to a final crustal thickness of 80 km and 20 km, respectively. Symbols are placed on the blue curve to indicate the FCMB where the open and closed symbol. The symbol color indicates the inner-core size. A square indicates that the inner core has not yet formed at 4.5 Gyr. The dashed horizontal lines indicate planetary contraction of 0, 2, and 7 km.

5. 前陶器至陶器新石器时期约旦古地磁强度变化

翻译人：柳加波 liujb@sustech.edu.cn

Di Chiara A, Tauxe L, Levy T E, et al. ***The strength of the Earth's magnetic field from Pre-Pottery to Pottery Neolithic, Jordan*** *[J]. Proceedings of the National Academy of Sciences, 2021, 118(34). https://doi.org/10.1073/pnas.2100995118*

摘要：地磁场的显著变化对地球深部活动和生命演化都具有重要意义。确切的地磁场变化也能用来定年。本文研究了约旦新石器时期的陶片和燧石记录的古地磁结果。这是黎凡特地区最古老的古地磁结果之一，涵盖了人类历史的巨变时期。这些数据进一步提升了古地磁曲线的分辨率，从而使其更好地应用于定年和理解地磁场变化。此外，本文研究发现燧石这种在旧石器和之后的时期普遍存在的材料具有研究古强度的潜力。

ABSTRACT: The Earth's magnetic field has changed significantly in the past with implications for related phenomena, such as deep-Earth processes and evolution of life. Accurate datasets of its past behavior also provide a dating tool. We present data from Neolithic ceramics and flint from Jordan. Our results are among the oldest in the Levant, covering a period of major changes in human history. The data help in refining the resolution of the archaeomagnetic curve, in turn enhancing its use as a dating tool and for understanding past field behavior. Moreover, we demonstrate the potential for the use of flint material, the most common raw material for the manufacturing of tools in the entire Paleolithic and younger periods, for archaeointensity investigations.

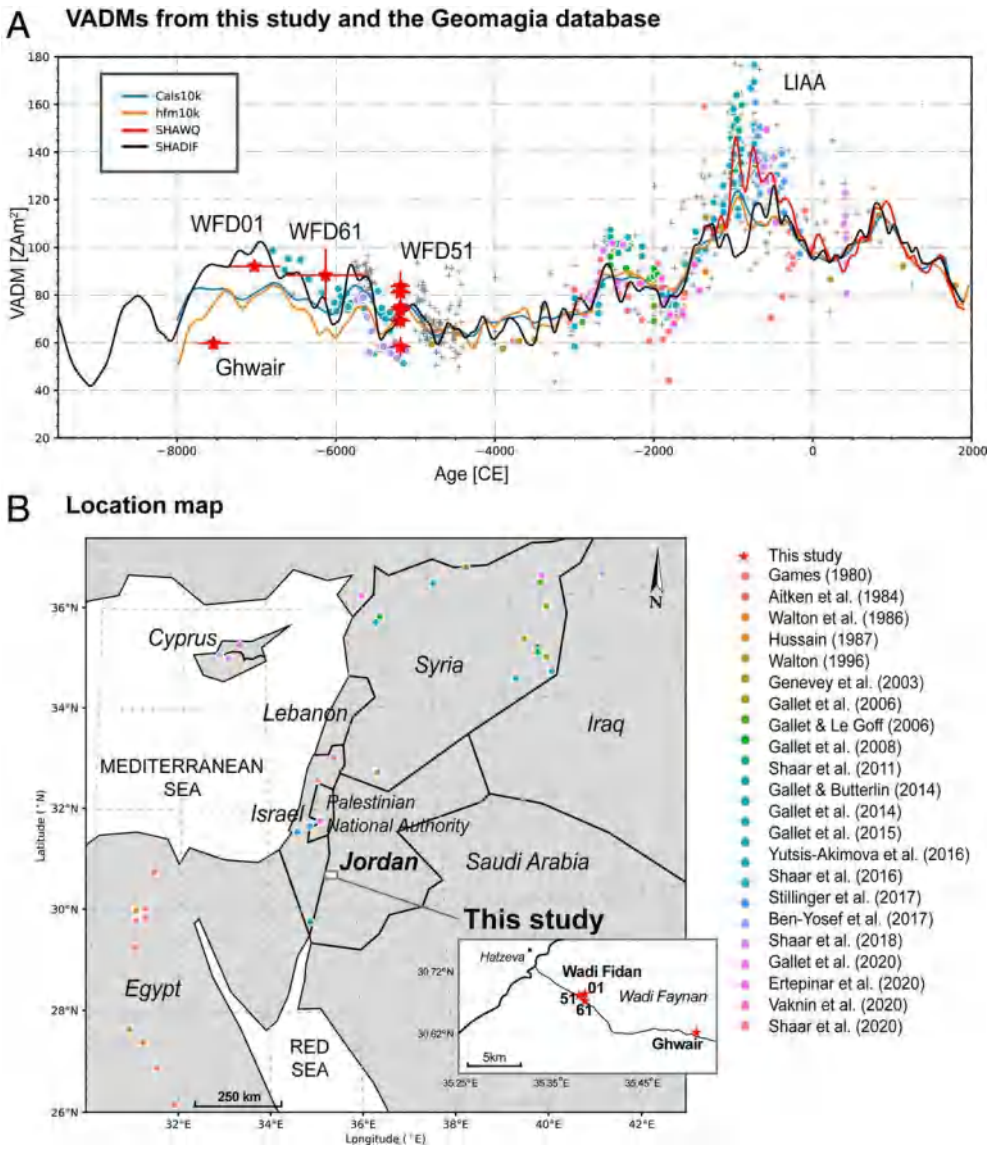

Figure 1. (*A*) Comparison between the results from the paleointensity analyses from this study (archaeointensity samples represented as red stars) and the data from previous studies available in the GEOMAGIA50 (ref. 34; gray crosses for the data that are not deemed robust), expressed as VADM in ZAm^2 ($=10^{21}Am^2$). The blue and orange curves are the two synthetic PSV curves from Cals10k.2 and hfm10k global models (35), respectively, and the black and red curves represent the two PSV curves from SHA.DIF.14K (36) and SHAWQ2k (26, 37), respectively, calculated at the coordinates of the study area. (*B*) Location of archaeointensity data from literature used in *A*. (*Inset*) Location of the four archaeological excavations of this study (the Wadi Faynan region, Jordan).

6. 过去 1 个百万年塞尔维亚北部黄土-古土壤矿物磁性特征

翻译人：张琪 zhangq7@sustech.edu.cn

Namier N, Gao X, Hao Q, et al, ***Mineral magnetic properties of loess–paleosol couplets of northern Serbia over the last 1.0 Ma*** *[J]. Quaternary Research, 2021, 1-14. https://doi.org/10.1017/qua.2021.41*

摘要：此研究首次对塞尔维亚 Titel-Stari Slankamen 黄土剖面的 9 个以上的黄土-古土壤序列进行了详细的矿物磁性特征研究，该剖面提供了欧洲自约 1.0 Ma 以来最长且最完整的古气候变化的陆地记录之一。研究结果表明，黄土中的亚铁磁性矿物以部分氧化的多域（MD）和假单域（PSD）磁铁矿为主；然而，随着成土作用程度的增加，风化作用产物逐渐被成土作用形成的超顺磁性（SP）和单畴（SD）亚铁磁性矿物（主要是磁铁矿）所掩盖。亚铁磁性矿物颗粒粒度的总体一致性表明，尽管在过去 1.0 Ma 的气候条件发生了变化，但细粒亚铁磁性矿物组分没有溶解。归一化的 $dJ/dT_{@120K}$ 和归一化的 $\chi_{heating@530^\circ C}$ 的变化反映了在过去 1.0 Ma 期间冰期干旱程度的长期阶梯式增加，主要在大约 0.6-0.5 Ma。研究结果为今后利用塞尔维亚黄土磁性特征进行古气候重建提供了良好的基础。

ABSTRACT: We conducted the first detailed mineral magnetic investigation of more than nine loess–paleosol couplets of the composite Titel-Stari Slankamen loess section in Serbia, which provides one of the longest and most complete terrestrial record of paleoclimatic changes in Europe since ~1.0 Ma. The results show that the ferrimagnetic mineral assemblage of the loess units is dominated by partially oxidized multidomain (MD) and pseudo-single domain (PSD) magnetite; however, with an increasing degree of pedogenesis, the eolian contribution is gradually masked by pedogenic superparamagnetic (SP) and single-domain (SD) ferrimagnets (mainly maghemite). The overall consistency of ferrimagnetic grain-size parameters indicates an absence of dissolution of the fine-grained ferrimagnetic fraction despite changes in climate regime over the past 1.0 Ma. The variations of normalized $dJ/dT_{@120K}$ and normalized $\chi_{heating@530°C}$ reflect a long-term stepwise increase in aridity during glacials with a major step at ~0.6–0.5 Ma, over the last 1.0 Ma. Overall, the results provide an improved basis for the future use of the magnetic properties of Serbian loess

deposits for paleoclimatic reconstruction.

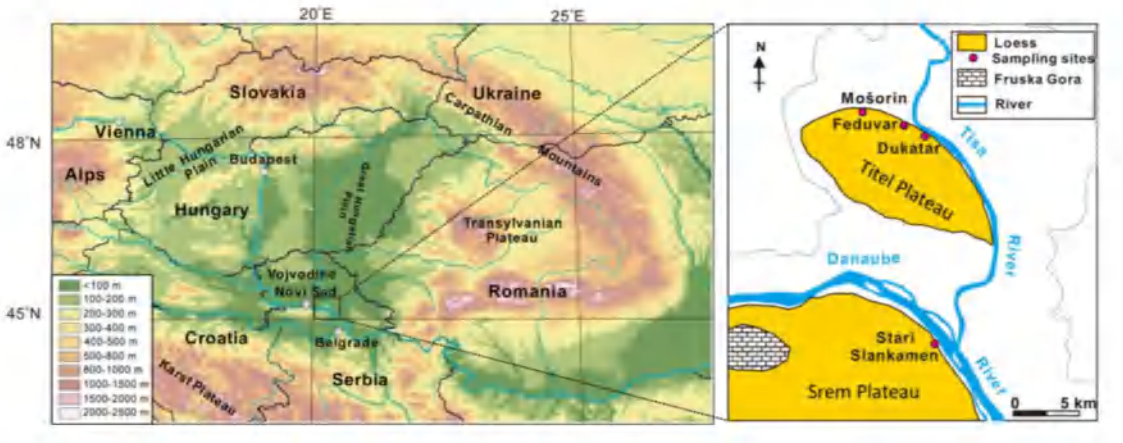

Figure 1. Location of the Titel-Stari Slankamen section, Serbia.

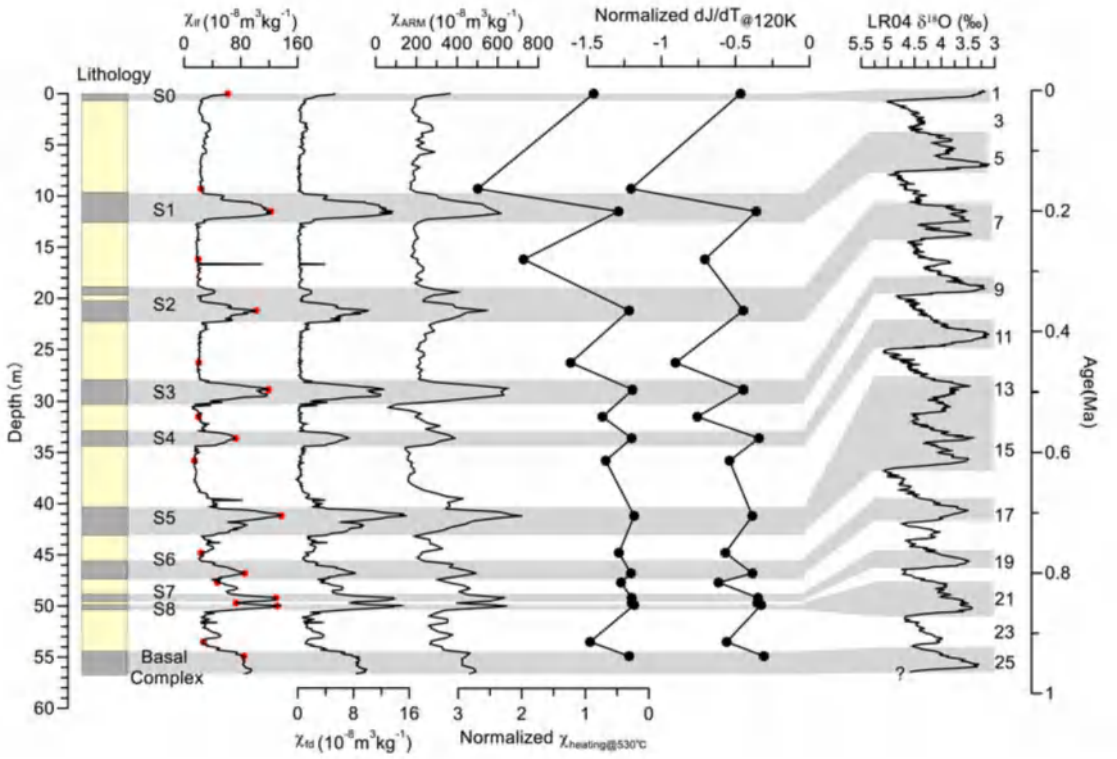

Figure 2. Stratigraphic variations of selected magnetic parameters of the composite Titel-Stari Slankamen loess–paleosol sequence and their correlation with the marine oxygen isotope record. The stratigraphic positions of the 19 samples for magnetic investigation are shown by solid circles on the magnetic susceptibility curve. See text for explanation of the proxies of normalized – $dJ/dT_{@120K}$ and normalized $\chi_{heating@530°C}$.

7. 华北克拉通东部侏罗纪基性岩浆弧的识别：古太平洋板块西向俯冲的地球化学证据

翻译人：周洋 zhouy3@sustech.edu.cn

Fang W, Dai L Q, Zheng Y F, et al. ***Identification of Jurassic mafic arc magmatism in the eastern North China Craton: Geochemical evidence for westward subduction of the Paleo-Pacific slab*** *[J]. Geological Society of America Bulletin, 2021, 133, 1404–1420.*

https://doi.org/10.1130/B35787.1

摘要：古太平洋板块向华北克拉通（NCC）之下的俯冲对克拉通的破坏产生了重要影响。然而，在 NCC 东部没有识别出可靠的安第斯型弧岩浆作用。在这里，我们报告了辽东半岛类似侏罗纪岩浆弧的煌斑岩，提供了早中生代古太平洋向 NCC 下方俯冲的证据。煌斑岩的锆石 U-Pb 定年为 158-155 Ma，为岩浆结晶年龄。这些煌斑岩都表现出典型的岛弧微量元素分布模式，但在放射性同位素组成和其他地球化学特征方面表现出一系列差异。1 型煌斑岩显示出 $(^{87}Sr/^{86}Sr)_i$ 比值为 0.7075–0.7085，εNd(t) 值为 -3.9 至 -1.3，εHf(t) 值为 -5.4 至 -0.3，而 2 型煌斑岩显示出中等富集的放射性同位素，$(^{87}Sr/^{86}Sr)_i$ 比值为 0.7096–0.7117，εNd(t) 值为 -12.2 至 -7.6，εHf(t) 值为 -12.8 至 -4.7。两类煌斑岩的锆石 Hf 同位素和全岩 Ba/Th、Ba/La、Sr/Nd、Th/Nd、Th/Yb 和 La/Sm 比值也存在系统差异。综上所述，这些异同可以通过克拉通地幔楔的交代反应来解释，该地幔楔具有源自俯冲古太平洋板块的两种流体特征。一种流体是俯冲的玄武质洋壳，另一种是俯冲的陆源熔融。俯冲带流体的两种特性以不同的比例混合到这些煌斑岩的地幔源中，因此，煌斑岩来源于交代地幔。这种解释得到了古海洋俯冲带板片-地幔界面地球化学转换定量模拟的验证。因此，华北克拉通东部侏罗纪煌斑岩为古太平洋板块俯冲过程中的壳幔相互作用提供了地球化学证据。早中生代，板块俯冲产生的流体交代作用会减弱克拉通地幔，在早白垩世发生减薄和破坏。

ABSTRACT: Subduction of the Paleo-Pacific slab beneath the North China Craton (NCC) has exerted a strong influence on the Mesozoic destruction of the craton. However, no Andean-type arc magmatism has been reliably identified in the eastern NCC. Here we report the occurrence of Jurassic arc-like lamprophyres in the Liaodong Peninsula, providing a snapshot of the Paleo-Pacific slab subduction beneath the NCC in the early Mesozoic. Zircon U-Pb dating of the lamprophyres yields consistent ages

of 158–155 Ma for magma crystallization. These lamprophyres all exhibit typical arc-like trace element distribution patterns, but show a series differences in their radiogenic isotope compositions and the other geochemical variables. Type 1 lamprophyres exhibit weakly enriched Sr-Nd-Hf isotopes with $(^{87}Sr/^{86}Sr)_i$ ratios of 0.7075–0.7085,εNd(t) values of −3.9 to −1.3 and εHf(t) values of −5.4 to −0.3, whereas Type 2 lamprophyres exhibit moderately enriched radiogenic isotopes with $(^{87}Sr/^{86}Sr)_i$ ratios of 0.7096–0.7117, εNd(t) values of −12.2 to −7.6 and εHf(t) values of −12.8 to −4.7. There are also systematic differences in zircon Hf isotopes and whole-rock Ba/Th, Ba/La, Sr/Nd, Th/Nd, Th/Yb, and La/Sm ratios for the two types of lamprophyre. Taken together, these similarities and differences can be accounted for by metasomatic reaction of the cratonic mantle wedge with two properties of liquid phase derived from subducting Paleo-Pacific slab. One is aqueous solutions from the subducting basaltic oceanic crust, and the other is hydrous melts from the subducting terrigenous. The two properties of subduction zone fluids were incorporated in different proportions into the mantle sources of these lamprophyres. Accordingly, the lamprophyres were derived from the metasomatic mantle sources. This qualitative interpretation is verified by quantitative modeling of the geochemical transfer at the slab-mantle interface in a paleo-oceanic subduction zone. Therefore, the Jurassic lamprophyres in the eastern NCC provide the geochemical evidence for the crust-mantle interaction during the Paleo-Pacific slab subduction beneath eastern Asia in the early Mesozoic, when the chemical metasomatism by the slab-derived fluids would have weakened the cratonic mantle for its thinning and destruction in the Early Cretaceous.

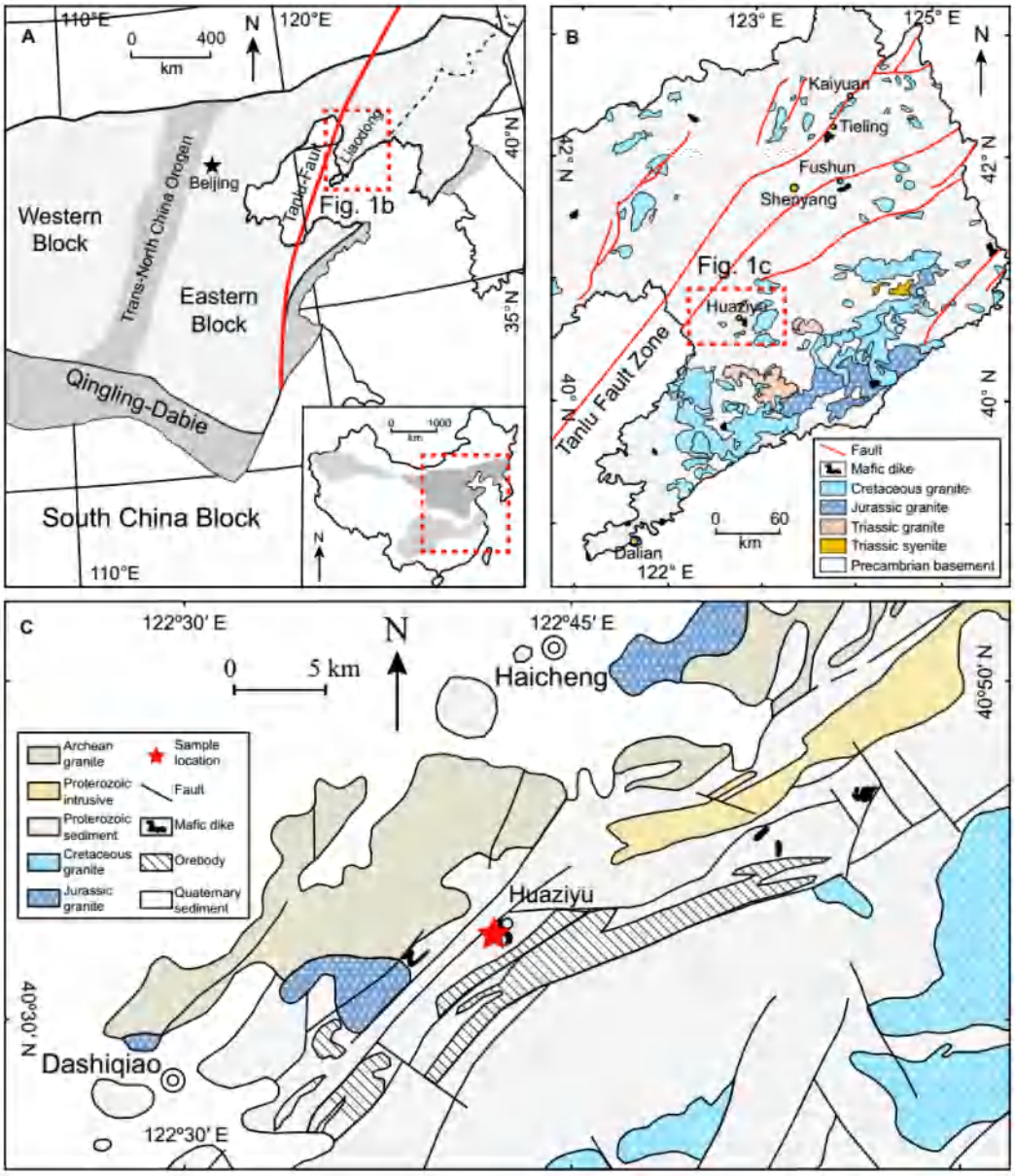

Figure 1. (A) Simplifed geological maps of the study area, showing main tectonic units of the North China Craton (modified after Zhu et al., 2012). (B) Distribution of Mesozoic magmatism in the Liaodong Peninsula, the eastern North China Craton (modified after Ma et al., 2002). (C) Geological map of the Huaziyu area, showing the distribution of mafic dikes and sample locations (modified after Ma et al., 2002).

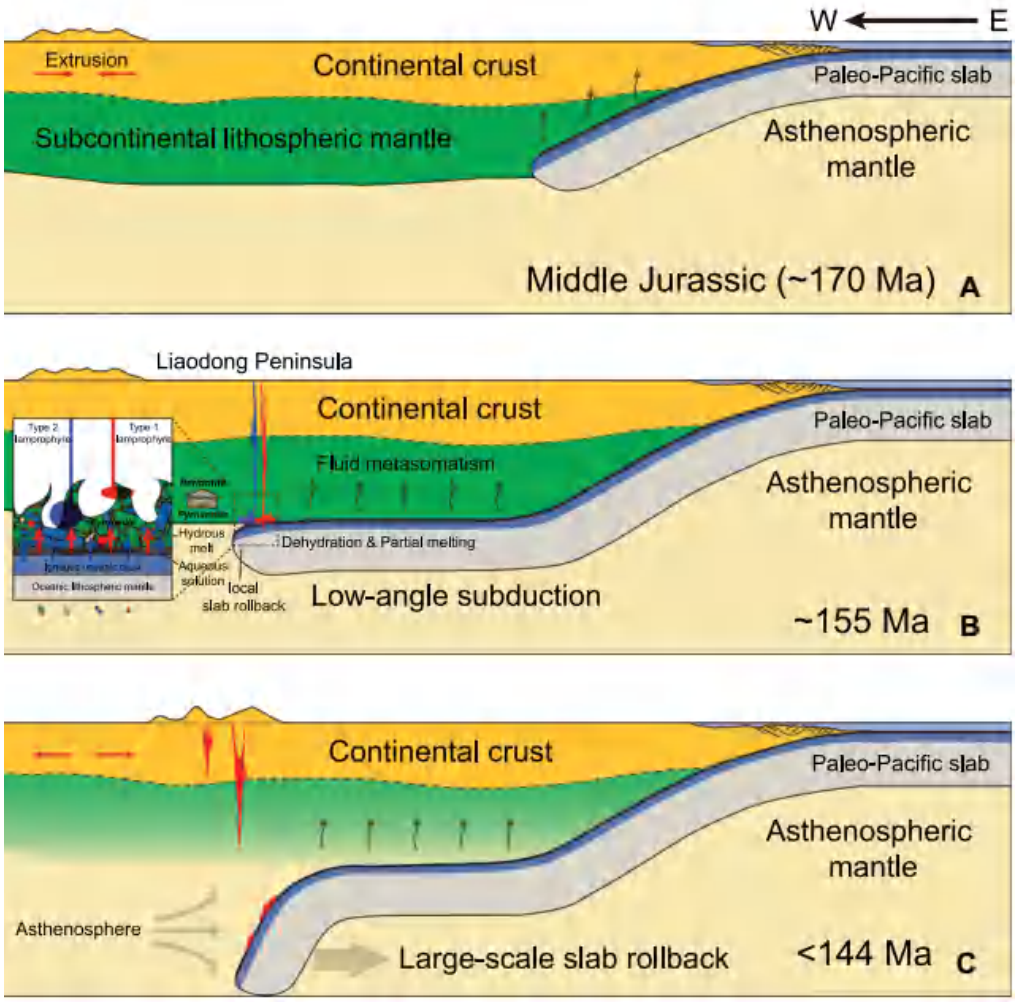

Figure 2. Schematic illustration for the subduction of the Paleo-Pacific slab and its consequence on the origin of lamprophyres in the eastern North China Craton. (A) In the Middle Jurassic (ca. 170 Ma), the Paleo-Pacific slab started to subduct beneath eastern Asia. (B) The sub-continental lithosphere mantle (SCLM) of the North China Craton (NCC) was chemically weakened by Paleo-Pacific slab-derived fluids during the low-angle subduction. The metasomatic reaction between the SCLM wedge peridotite and the Paleo-Pacific slab derived fluids would have generated lithologically fertile, geochemically enriched mantle domains, whose partial melting at ca. 155 Ma to generated two types of lamprophyre due to the local slab rollback. (C) After ca. 144 Ma, the subducting Paleo-Pacific slab started large scale rollback, leading to lateral flow of the asthenospheric mantle onto the base of the NCC for heating. This gave rise to the voluminous bimodal magmatism at 130–120 Ma.

8. 气候变暖导致布伦特冰架不稳定性增加，加速了冰川裂解的到来

翻译人：盖聪聪 gaicc@sustech.edu.cn

Cheng Y, Xia M, Qiao G, et al. ***Imminent calving accelerated by increased instability of the Brunt Ice Shelf, in response to climate warming*** *[J]. Earth and Planetary Science Letters, 2021(572). https://doi.org/10.1016/j.epsl.2021.117132*

摘要：南威德尔海具有覆盖范围广且体积大的冰架。由于冰架位于寒冷的近表层和次表层水体，前人研究认为这些冰架很稳定。布伦特冰架（BIS）是距离大陆架坡折最近的冰架之一，在 2021 年二月下旬释放了 1270 km^2 的冰川，另一个大冰川崩解事件也即将发生。然而，对 2017 年以来布伦特冰架的演化缺乏研究。作者通过多源遥感数据（包括卫星图像、冰流速度积、数字高程模型和高程数据）的分析得出冰架不稳定性逐渐增加的结论。增加的冰流速度和全层裂缝传播速率表明不稳定性增加。布伦特冰架前缘从 2013 年到 2021 年的速率增大了 2 倍以上, Chasm 1 的宽度在 2012 到 2021 年增加到原来的三倍左右。根据 Chasm 1 的扩张以及应变率的改变，作者预计布伦特冰架可能在 2022 年 10 月的时候释放 1675 km^2 左右的冰川。作者通过对气象数据、海洋和野外观测的分析，认为暖流注入大陆架导致了布伦特冰架不稳定性增加，作者还强调了进一步观察和分析的重要性。此外，由于布伦特地理位置特殊，它可以用来指示南威德尔海其它冰架的演化。

ABSTRACT: Ice shelves in the Southern Weddell Sea have large areas and volumes, and have previously been stable due to their setting in a region of cold near-surface and sub-surface ocean water. The Brunt Ice Shelf (BIS), one of the ice shelves closest to the continental shelf break in the region, just released an iceberg with an area of ~1,270 km^2 in late February 2021 and another large calving event is imminent. However, recent changes in the BIS, since 2017, have not been studied to date. In this study, we used multi-source remote sensing data (including satellite images, ice flow velocity products, digital elevation models, and altimetry data) to conclude that the instability of the ice shelf has been increasing. The increased instability is manifested by rapidly increasing ice flow velocity and the propagation rate of full-thickness rifts. The velocity at the front of the BIS accelerated by more than doubled from 2013–2021, and the width of Chasm 1 increased by almost three-fold from 2012–2021. Based on the expansion

of Chasm 1 and the strain rate changes, an iceberg with an area of ~1,675 km^2 is predicted to be released from the BIS during October 2022. We used meteorological data, ocean synthesis, and field observations to attribute the increased instability of the BIS to warm inflow onto the continental shelf, which emphasizes the importance of further observation and analysis. Additionally, owing to its special location, the BIS could be an indicator of the evolution of other ice shelves in the Southern Weddell Sea.

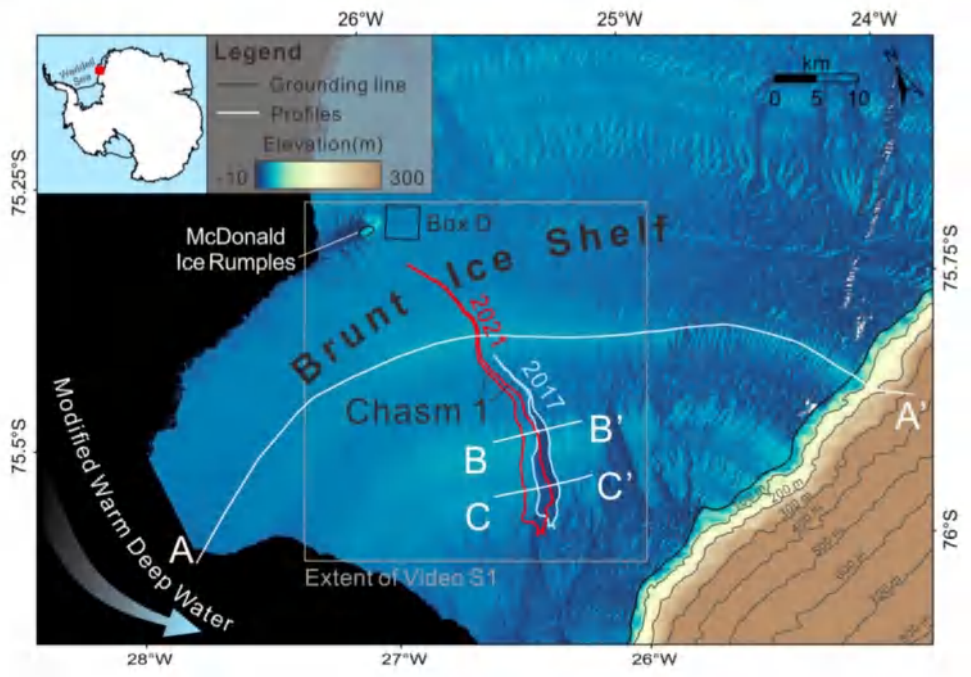

Figure 1. Map of the BIS with inset in the upper left corner showing the ice shelf location. The background is an 8-m REMA-DEM tile product (2011-2017) overlaid by an 8-m REMA DEM strip product of 2017, on which the Chasm 1 can be clearly observed. All these DEMs are reference to WGS84 ellipsoid. The dark grey lines are contours. Light blue and red polygons represent the locations of Chasm 1 in 2017 and 2021, respectively. The white lines along the ice flow illustrate the locations of three profiles (AA', BB', and CC'), and the black line is the grounding line from Rignot et al. (2011a). The arrow at the lower left represents the direction of the Modified Warm Deep Water (MWDW; Ryan et al., 2020). The grey polygon is the extent of Video S1, and Box D is the extent for generating the longitudinal strain rate time series.

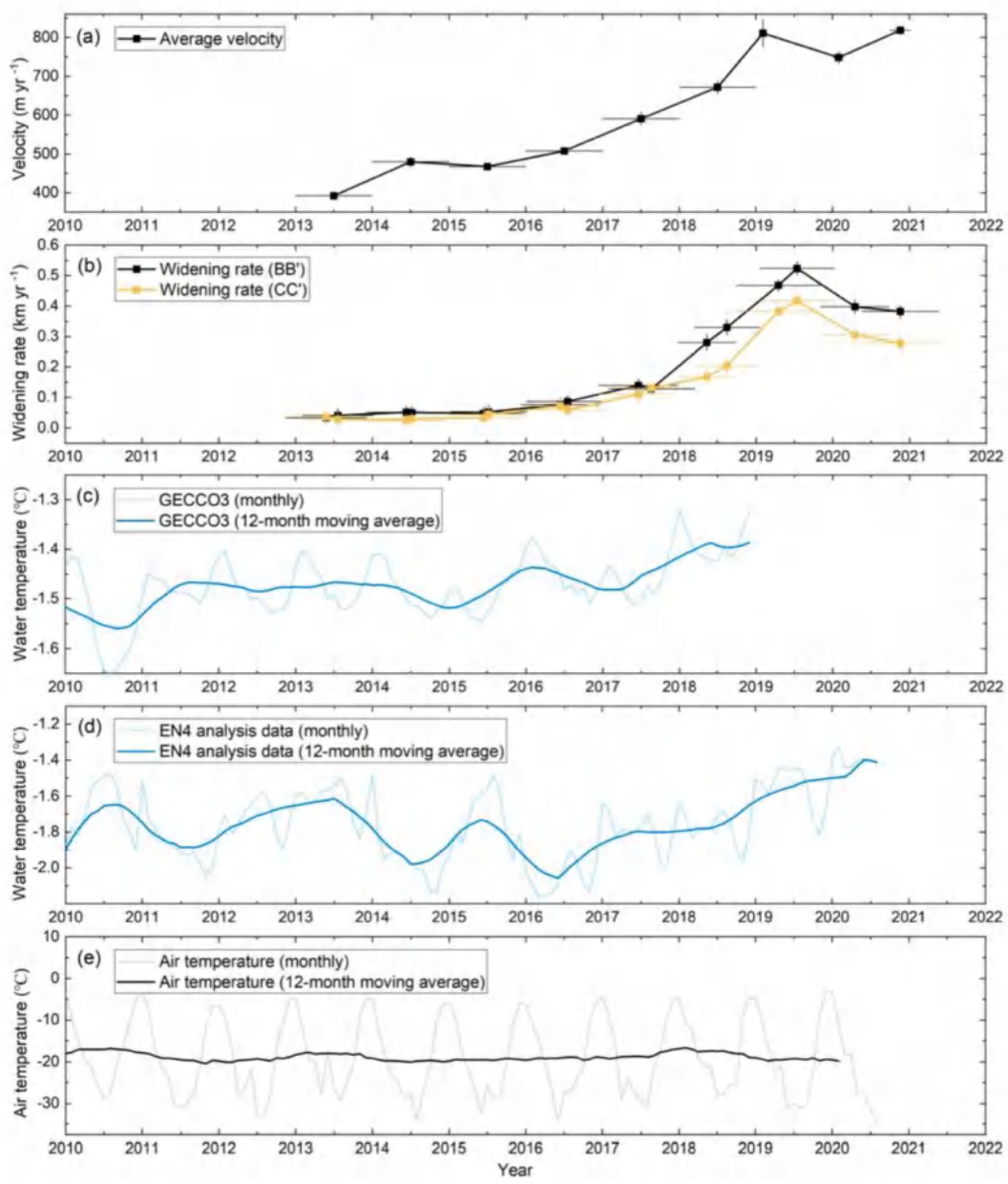

Figure 2. (a) Time series of averaged velocity at the seaward part of Profile AA' from 2013– 2021; (b) widening rates of Chasm 1 along BB' and CC' from 2012–2021;(c) potential water temperature from GECCO3 and values smoothed with a 12-month moving filter; (d) potential water temperature from EN4 and values smoothed with a 12-month moving filter;(e) air temperature at Halley Station and values smoothed with a 12-month moving filter.

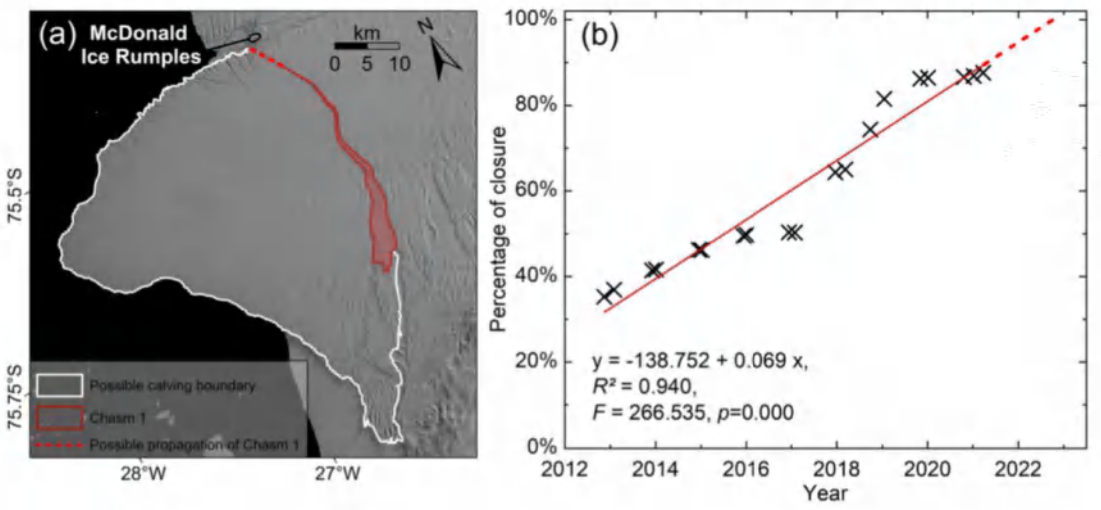

Figure 3. (a) Possible iceberg detachment boundary (white) and Chasm 1 (red) extracted from an OLI image taken on January 7, 2021. The red dashed line is the possible propagation route for Chasm 1; (b) calculated percentages (black crosses) used to establish the linear regress model (red line).

9. 基于ROV定向岩心的古地磁数据推断的菲律宾海板块旋转过程

翻译人：刘伟 inewway@163.com

Yamazaki T, Chiyonobu S, Ishizuka O, et al. ***Rotation of the Philippine Sea plate inferred from paleomagnetism of oriented cores taken with an ROV-based coring apparatus*** *[J]. Earth, Planets and Space, 2021, 73(1): 1-10.*

https://doi.org/10.1186/s40623-021-01490-5

摘要：重建菲律宾海(PHS)板块运动的历史对更好地理解周围板块的构造是十分重要的。一般认为 PHS 板块自始新世以来北移，但其旋转并未受到很好的约束;一些重建模型包含了大的顺时针旋转，但其他模型没有包含大的顺时针旋转。这主要是因为很难从处于水下的 PHS 板块收集定向岩石，阻碍了建立可靠的视极移曲线。在本研究中，我们使用基于 ROC 取芯设备对位于九州-帕劳脊（PHS 板块内部稳定的残余弧）北部的海山进行了定向岩心的古地磁研究。对 2 个~ 30 cm 长的中晚渐新世石灰岩岩心进行了逐步热退磁和交变磁场退磁处理，分离出特征剩磁方向。取两个岩心的平均古地磁偏角和倾角为 D = 51.5, I = 39.8。中晚渐新世以来的偏东偏角意味着 PHS 板块顺时针旋转约 50° 。此外，还根据平均倾角估算了 PHS 板块约 5 个纬度的变化。结果表明，中-晚渐新世九州-帕劳洋脊位于现今位置的西南侧，PHS 板块的旋转以及四国盆地和帕里西维拉盆地的扩张导致了伊豆-小笠原弧向东迁移至现今位置。

ABSTRACT: Reconstructing the history of Philippine Sea (PHS) plate motion is important for better understanding of the tectonics of the surrounding plates. It is generally considered that the PHS plate migrated northward since Eocene, but its rotation has not been constrained well; some reconstructions incorporated a large clockwise rotation but others did not. This is mainly because the difficulty of collecting oriented rocks from the mostly submerged PHS plate hindered establishing an apparent polar wander path. In this study, we conducted a paleomagnetic study of oriented cores taken using an ROV-based coring apparatus from the Hyuga Seamount on the northern part of the Kyushu-Palau Ridge, a remnant arc in the stable interior of the PHS plate. Stepwise thermal and alternating-field demagnetizations were applied to specimens taken

successively from two ~ 30 cm long limestone cores of middle to late Oligocene age, and characteristic remanent magnetization directions could be isolated. Declination and inclination of D = 51.5° and I = 39.8°, respectively, were obtained as the mean of the two cores. The easterly-deflected declination means ~ 50° clockwise rotation of the PHS plate since middle to late Oligocene. In addition, ~ 5° latitudinal change of the site is estimated from the mean inclination. The result implies that the Kyushu-Palau Ridge was located to the southwest of the present position in middle to late Oligocene, and that PHS plate rotation as well as the Shikoku and Parece Vela Basin spreading contributed to the eastward migration of the Izu-Ogasawara (Bonin) Arc to the current position.

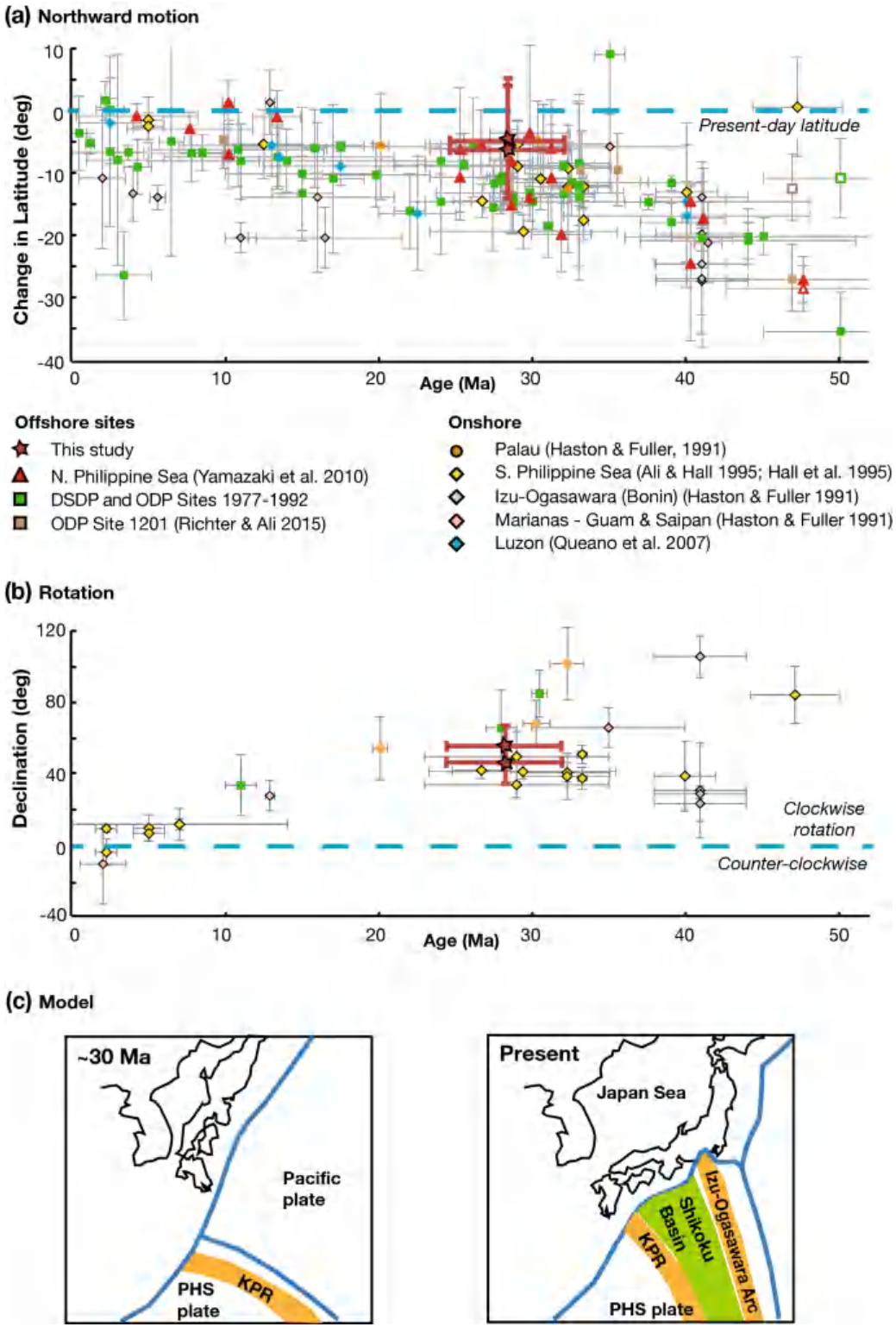

Figure 1. Latitudinal change (a) and rotation (b) of the Philippine Sea plate with age compiled from published studies (Wu et al. 2016, Fig. 3) and the present study (red star). References for DSDP and ODP Sites in 1977–1992 are Louden (1977), Kinoshita (1980), Keating and Herrero (1980), Keating (1980), Bleil (1982), Haston et al. (1992), and Koyama et al. (1992). c Schematic model of the Kyushu-Palau ridge (KPR) location at ~ 30 Ma (left) and the present positions of KPR and Izu-Ogasawara (Bonin) arc (right).

10.中国东部降雨在过去 425ka 的三极模型的模拟研究

翻译人：杨会会 11849590@mail.sustech.edu.cn

Dai G W, Zhang Z S, Ottera O H, et al., ***A Modeling Study of the Tripole Pattern of East China Precipitation Over the Past 425 ka*** *[J]. Journal of Geophysical Research: Atmospheres ,2021, 126, e2020JD033513.*

https://doi.org/10.1029/2020JD033513

摘要：传统的古气候学观点认为，东亚夏季风强时，中国季风区总体偏湿。然而，这一观点与现代气候的理解不一致，现代气候表明在中国季风区气候类似于“三极降水模式”。我们对中国季风区古降雨的空间格局所知甚少，特别是过去的冰期-间冰期旋回的降雨空间格局。在此，我们利用气候模式为过去 425 ka 中国季风区潜在的三极降水模式提供了证据，并将结果与中国的古气候记录进行了比较。结果表明，东亚夏季风强（弱）期华北和华南降水偏多（偏少)，中东部降水偏少（偏多），这与与北方夏季高（低）日照有关。我们的研究结果与现代东亚气候的认识一致，并进一步证实了北方夏季日照是东亚夏季风强度的主导驱动因素，在轨道时间尺度上副热带高压的响应是调节中国季风区降水模式的基础。模拟结果表明，在过去的冰期-间冰期旋回中，中国季风区降雨的时空变化具有高度的复杂性。然而，过去 425 ka 中国季风区的三极降水模式是否足够强还需要检验，最好利用中国中东部现有的和新的，具有精确定年的和明确降雨指示意义的记录。

ABSTRACT: The traditional paleoclimatological view suggests that monsoonal China was overall wetter when the East Asian summer monsoon (EASM) was strong. However, this view is at odds with the understanding of modern climate, which demonstrates an analogous “tripole precipitation pattern” in monsoonal China. Little is known about the spatial pattern of paleo-precipitation in monsoonal China, particularly during the past glacial-interglacial cycles. Here, we provide evidence for a potential tripole precipitation pattern in monsoonal China over the past 425 ka using climate modeling, and compare the results with paleoclimate records available from China. Our simulations illustrate that more (less) precipitation in North China and South China, and less (more) precipitation in the Central-East China during strong (weak) EASM periods associated with high (low) boreal

summer insolation. Our results agree with the present understanding of modern East Asian climate, and furthermore confirm that the boreal summer insolation is the dominant forcing for the intensity of EASM and the response of subtropical high pressures is fundamental in modulating the precipitation pattern in monsoonal China on orbital timescales. This temporal and spatial variability of precipitation, as revealed in our simulations, shows the potential high complexities in hydroclimatic conditions in monsoonal China throughout the past glacial-interglacial cycles. Nevertheless, whether the tripole precipitation pattern in monsoonal China over the past 425 ka is robust enough still should be tested, preferable by taking advantage of existing and new well-dated and explicit indicative precipitation archives in Central-East China.

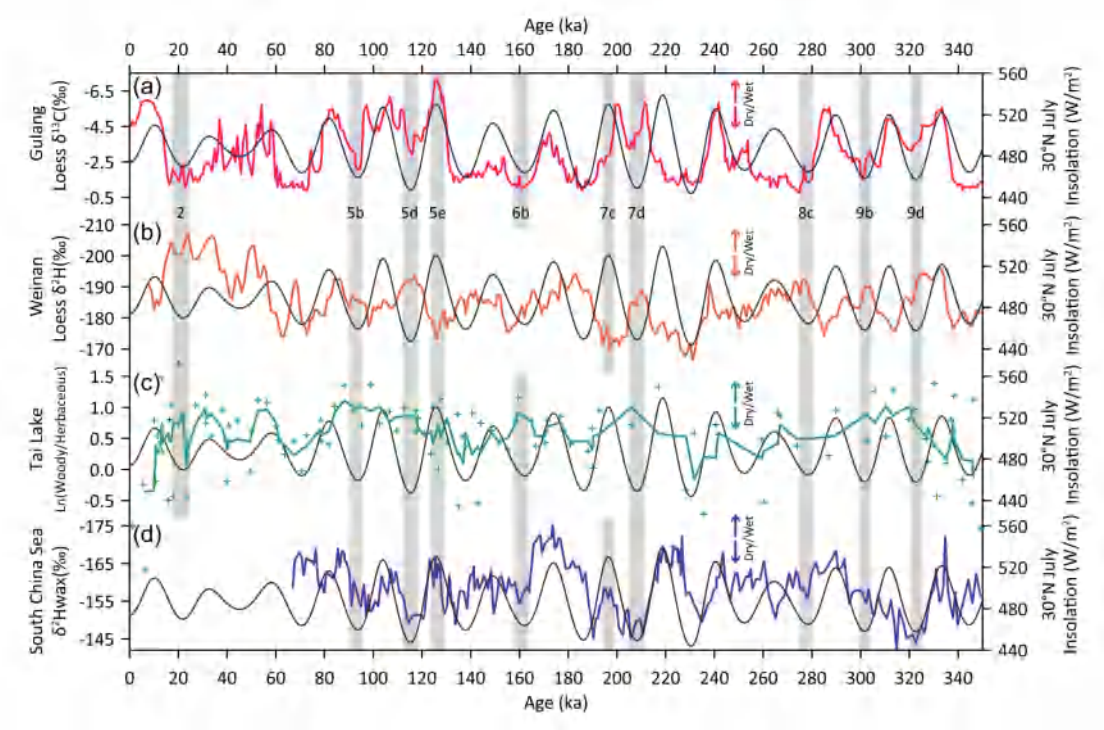

Figure 1. Potential dry and wet climate state reflected by geological records. (a) Loess $\delta^{13}C$ from Gulang (37.48°N, 102.87°E, North China; Sun et al., 2015). (b) Loess $\delta^{2}H_{wax}$ from Weinan (34.42°N, 109.6°E, south margin of Chinese Loess Plateau, near Central-East China; Thomas, Clemens, Sun, et al., 2016). (c) The pollen ratio of Woody/Herbaceous from Tai Lake (31.5°N, 120.45°E, Central-East China; Miao et al., 2015), the green curve is the result of original pollen ratios (green crosses) by three-point moving average. (d) The marine sediment biomarker records $\delta^{2}H_{wax}$ from ODP Site 1146 (19.45°N, 116.27°E, South China; Thomas, Clemens, Prell, et al., 2014). The black curves represent 30°N July insolation

(Laskar et al., 2004), and gray bars indicate the stages of resembling tripolar precipitation pattern. Here, for (a, b, and d), the chronologies are based on the radiometrically calibrated age model, the control point ages are mainly from comparison between the mean grain size of loess or benthic $\delta^{18}O$ of marine sediments and the standard benthic $\delta^{18}O$ (Lisiecki & Raymo, 2005) or well dated speleothem records; for (c), the chronologies are obtained by the linear interpolation between the ^{14}C age and B/M boundary (780 ka).

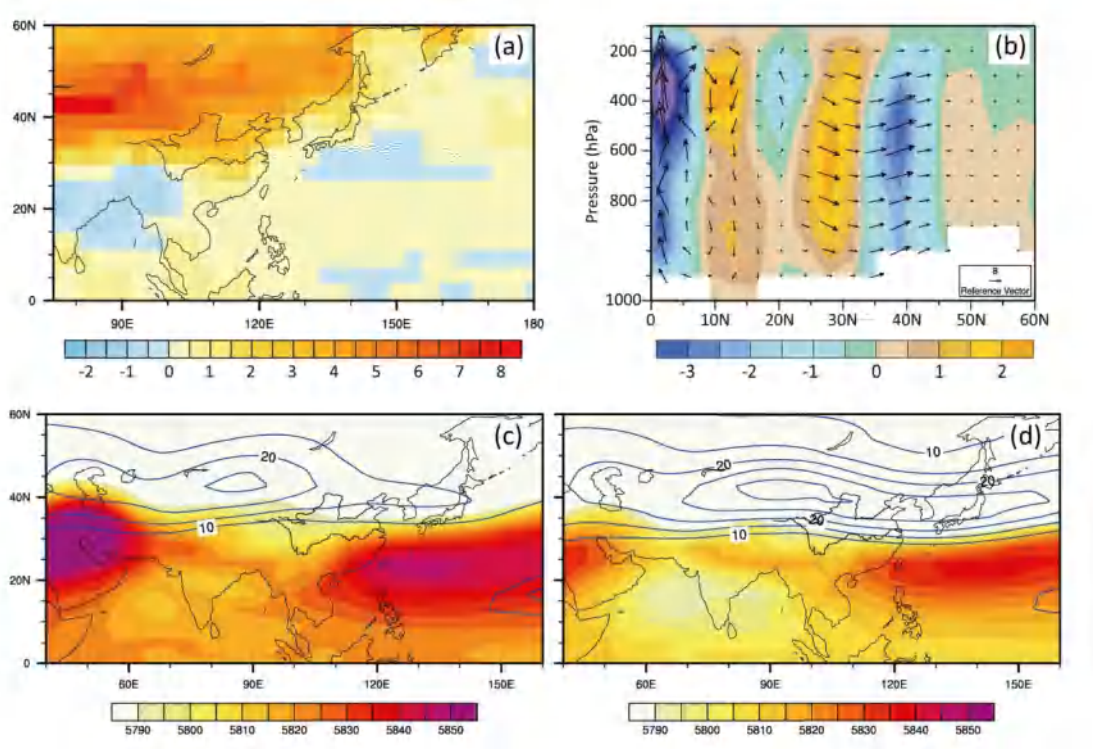

Figure 2. The simulated ensemble mean climatic anomaly due to intensified summer monsoon (20 insolation maxima minus 20 insolation minima). (a) The anomaly summer (JJA) surface temperature (°C). (b) The shading colors show the 115°E anomaly summer (JJA) vertical movement (Omega, which is magnified by one hundred times, unit: Pa/s; and the positive value indicates enhanced descending motion); the vector arrows indicate the 115°E anomaly JJA meridional wind (V, unit: m/s) and vertical movement (Omega, magnified by 700, unit: Pa/s). For (c and d), blue contour lines show the summer (JJA) zonal wind (U, unit: m/s, ≥10 m/s displayed) at 200 hPa, indicating the westerly jet; the shading colors show the summer (JJA) geopotential height (unit: gpm) at 500 hPa, indicating the western Pacific subtropical high. Here, (c) is for the maximal insolation periods and (d) is for the minimal insolation periods.

11. 在西太平洋边缘海域用基于小波和傅立叶谱质心法估算居里点深度

翻译人：曹伟 11930854@qq.com

Yin Y, Li C F, Lu Y. ***Estimating Curie-point depths using both wavelet-based and Fourier spectral centroid methods in the western Pacific marginal seas*** *[J]. Geophysical Journal International, 2021, 227(2):798-812.*

https://doi.org/10.1093/gji/ggab257

摘要：居里点深度是研究岩石圈地质结构和热演化的重要磁学参数。在本研究中，我们首先将小波变换应用于质心法，并将其与基于三维分形磁化模型的传统傅里叶谱质心法进行比较。我们发现傅里叶变换方法适用于估计较小的居里点深度（小于 20km），而小波变换方法在估计较大的居里点深度（大于 30km）时具有更好的精度。将这两种方法应用于 2-arcmin 分辨率地球磁异常网格（EMAG2）的西太平洋磁异常，证明了它们的可靠性和可比性。我们的结果表明，在岩浆活动活跃和高热流的地区，如大洋中脊和俯冲带岛弧，居里点深度较小，但在沉积盆地和俯冲带前段，表面热流较低，居里点深度较大。我们使用 FORTRAN 语言编写了居里点深度反演软件 CPDINV，该软件包括最小曲率网格、投影、小波和傅里叶变换、最小二乘拟合和深度估计等完整模块。

ABSTRACT: The Curie-point depth is an important magnetic parameter for studying the geological structure and thermal evolution of the lithosphere. In this study, we first apply wavelet transform to the centroid method, and compare it with the conventional Fourier spectral centroid method based on a 3-D fractal magnetization model. We find that the Fourier transform method is suitable for estimating smaller Curie-point depths (less than 20 km), whereas the wavelet transform method has better accuracy in estimating large Curie-point depths (more than 30 km). The application of both methods to the western Pacific magnetic anomalies from the Earth Magnetic Anomaly Grid of 2-arcmin resolution (EMAG2) proves their reliability and comparability. Our results show small Curie-point depths in areas with active magmatism and high heat flow, like mid-ocean ridges and island arcs of subduction zones, but large Curie-point depths in sedimentary basins

and forearcs of subduction zones with low surface heat flow. We wrote our Curie-point depth inversion software CPDINV using FORTRAN language, which includes completed modules of minimum-curvature gridding, projection, wavelet and Fourier transforms, least-squares fitting and depth estimation.

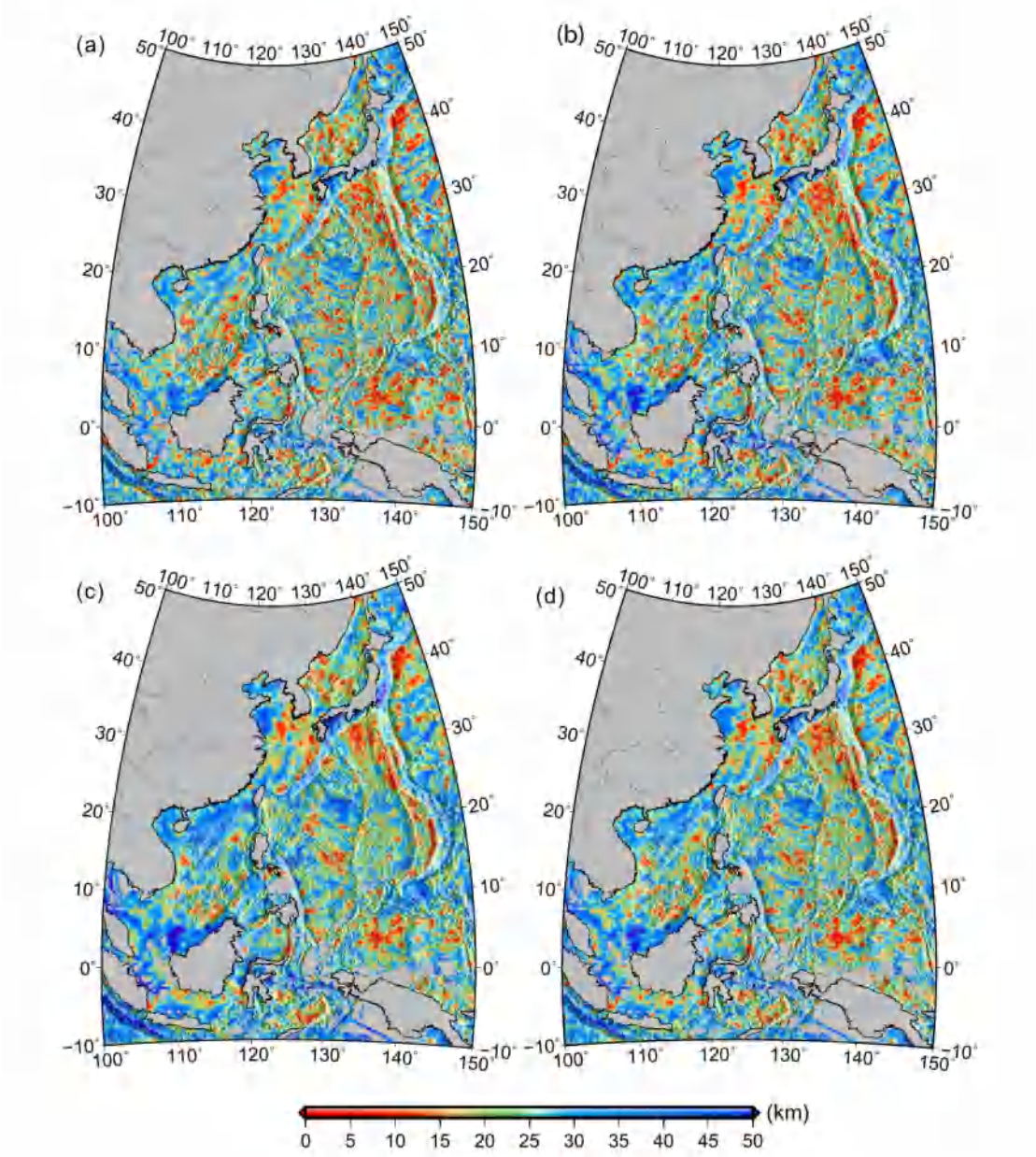

Figure 1. Map of Curie-point depths estimated from magnetic anomalies shown in Fig. 6(b) using centre wavenumbers of (a) k_0= 2.668, (b) k_0= 3.773 and (c) k_0= 5.336 with a constant 3-D fractal exponent of 3.0. (d) Averaged Curie-point depths from three different centre wavenumbers.

12. 渐新世气候之谜与全球地表温度演化

翻译人：王敦繁 Dunfan-w@foxmail.com

O'Brien C L, Huber M, Thomas E, et al. ***The enigma of Oligocene climate and global surface temperature evolution****[J]. Proceedings of the National Academy of Sciences, 2020, 117(41): 25302-25309.*

https://doi.org/10.1073/pnas.2003914117

摘要：大气中二氧化碳水平的下降导致始新世期间气温下降，并导致南极冰盖在渐新世（气候记录不佳的时期）开始扩张，接近现代规模。在这里，我们根据西南大西洋深海钻探项目站点 516（古纬度~ 36°S）和西赤道大西洋钻探项目站点 929（古纬度~ 0°）估算的 TEX_{86} 海表温度（SST），提出了整个渐新世（33.9 至 23.0 Ma）的气候演化记录。结合现有海温记录和气候模式的汇编。在这个二氧化碳含量相对较低的渐新世世界（约 300 - 700ppm），与始新世晚期相似的温暖气候继续存在，只有短暂的中断，而南极冰盖则时而活跃时而减弱。海温在空间上是不均匀的，但总体上支持晚渐新世变暖与大气 CO_2 下降相一致。这种渐新世的温暖，特别是在高纬度地区，掩盖了气候与大气 CO_2 和/或海洋通道之间的简单关系，目前的气候模型只能部分解释这一关系。虽然这个神秘的渐新世世界的主要气候驱动因素尚不清楚，但我们的研究结果有助于填补理解过去新生代气候的空白，以及长期气候敏感性对不同背景气候状态的响应方式。

ABSTRACT: Falling atmospheric CO_2 levels led to cooling through the Eocene and the expansion of Antarctic ice sheets close to their modern size near the beginning of the Oligocene, a period of poorly documented climate. Here, we present a record of climate evolution across the entire Oligocene (33.9 to 23.0 Ma) based on TEX_{86} sea surface temperature (SST) estimates from southwestern Atlantic Deep Sea Drilling Project Site 516 (paleolatitude ~36°S) and western equatorial Atlantic Ocean Drilling Project Site 929 (paleolatitude ~0°), combined with a compilation of existing SST records and climate modeling. In this relatively low CO_2 Oligocene world (~300 to 700 ppm), warm climates similar to those of the late Eocene continued with only brief interruptions, while the Antarctic ice sheet waxed and waned. SSTs are spatially heterogenous, but generally support late Oligocene warming coincident with declining atmospheric CO_2. This

Oligocene warmth, especially at high latitudes, belies a simple relationship between climate and atmospheric CO_2 and/or ocean gateways, and is only partially explained by current climate models. Although the dominant climate drivers of this enigmatic Oligocene world remain unclear, our results help fill a gap in understanding past Cenozoic climates and the way long-term climate sensitivity responded to varying background climate states.

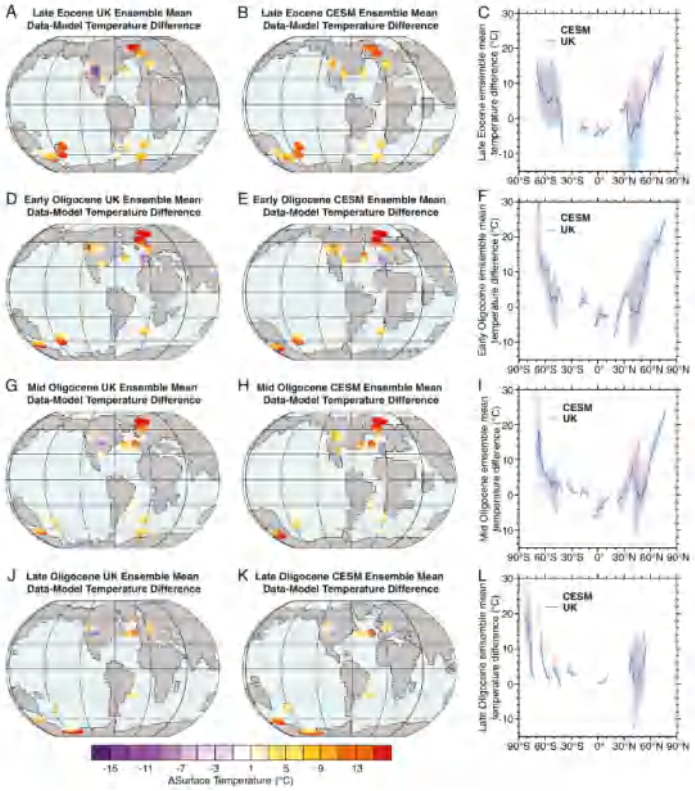

Figure 1. Eocene–Oligocene surface temperature data–model comparisons. (A–L) Surface temperature data–model comparisons for four Eocene–Oligocene time slices. Data–model comparisons are represented both spatially (A, B, D, E, G, H, J, and K) and as zonal mean of the differences versus latitude (C, F, I, and L). Differences in A, B, D, E, G, H, J, and K are calculated as the pointwise difference between the proxy mean value and model annual mean, then optimally interpolated and plotted as "circles" of difference. The shaded bands in C, F, I, and L represent minimum and maximum differences associated with the zonal means. Proxy data were compared to ensembles means from HadCM3L (UK) and CESM simulations. Modeling details are provided in SI Appendix, Table S1. Compiled Eocene–Oligocene surface temperature proxy data are shown in SI Appendix, Fig. S9. Refer to Methods and SI Appendix, Text 5, for further details.

13. 古 ENSO 对非洲环境和早期现代人类的影响

翻译人：李海 12031330@mail.sustech.edu.cn

Kaboth-Bahr S, Gosling W D, Vogelsang R, et al. ***Paleo-ENSO influence on African environments and early modern humans*** *[J]. Proceedings of the National Academy of Sciences, 2021, 118(23). https://doi.org/10.1073/pnas.2018277118*

摘要：本次研究，作者综合了 620 ky 以来陆地与海洋记录，用于解译泛非洲气候变异及其驱动因素与人类进化的潜在联系。作者发现整个非洲的水汽可用性与 ENSO 的变化密切相关，这是沃克环流的一种表现形式，这很可能是由地球离心率的变化驱动的。研究结果表明，低纬日照是驱动泛非洲中-晚更新世气候转变的主要因素。作者认为，这些低纬度气候过程通过增加资源丰富和稳定的生态环境，控制了非洲东部和西部的植被与哺乳动物的分布与进化，这些环境对早期现代人类很重要。

ABSTRACT: In this study, we synthesize terrestrial and marine proxy records, spanning the past 620 ky, to decipher pan-African climate variability and its drivers and potential linkages to hominin evolution. We find a tight correlation between moisture availability across Africa to El Niño Southern Ocean oscillation (ENSO) variability, a manifestation of the Walker Circulation, that was most likely driven by changes in Earth's eccentricity. Our results demonstrate that low-latitude insolation was a prominent driver of pan-African climate change during the Middle to Late Pleistocene. We argue that these low-latitude climate processes governed the dispersion and evolution of vegetation as well as mammals in eastern and western Africa by increasing resource-rich and stable ecotonal settings thought to have been important to early modern humans.

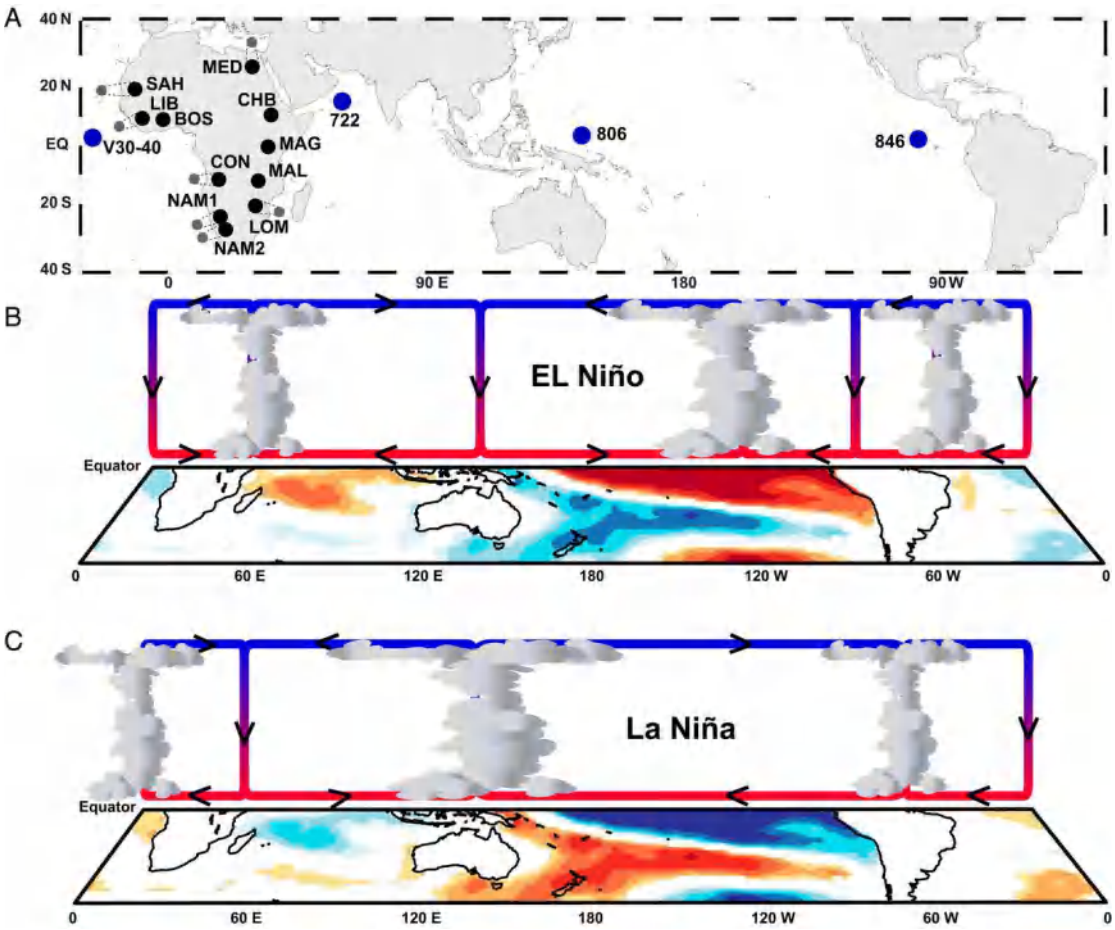

Figure 1. Suite of study sites and the global WC. (A) Location map of marine and terrestrial proxy records used for the reconstruction of African climate. Note that the black dots associated with marine sites (small gray dots) are referred to their respective hinterland region. SAH = Ocean Drilling Program (ODP) Site 659; LIB = ODP663; BOS = Lake Bosumtwi; CON = ODP Site 1075; NAM1 = GeoB1028-5; NAM2 = ODP Site 1082; LOM = MD96-2048; MAL = Lake Malawi; MAG = Lake Magadi; CHB = Paleolake Chew Bahir; and MED = ODP Site 967. The full list of references and coordinates for all sites is provided in SI Appendix, Table S1. Blue dots mark marine sites used for the reconstruction of the WC (SI Appendix, Table S2). (B) SST anomalies and resulting changes in tropical heating and convection (related to WC) under El Niño conditions (positive ENSO phase). (C) SST anomalies and resulting changes in tropical heating and convection (related to WC) under La Niña conditions (negative ENSO phase). For more details on the effect of El Niño/La Niña on African precipitation, see SI Appendix. Blue areas = cooling relative to normal conditions; red areas = warming relative to normal conditions; and black arrows indicate transport direction.

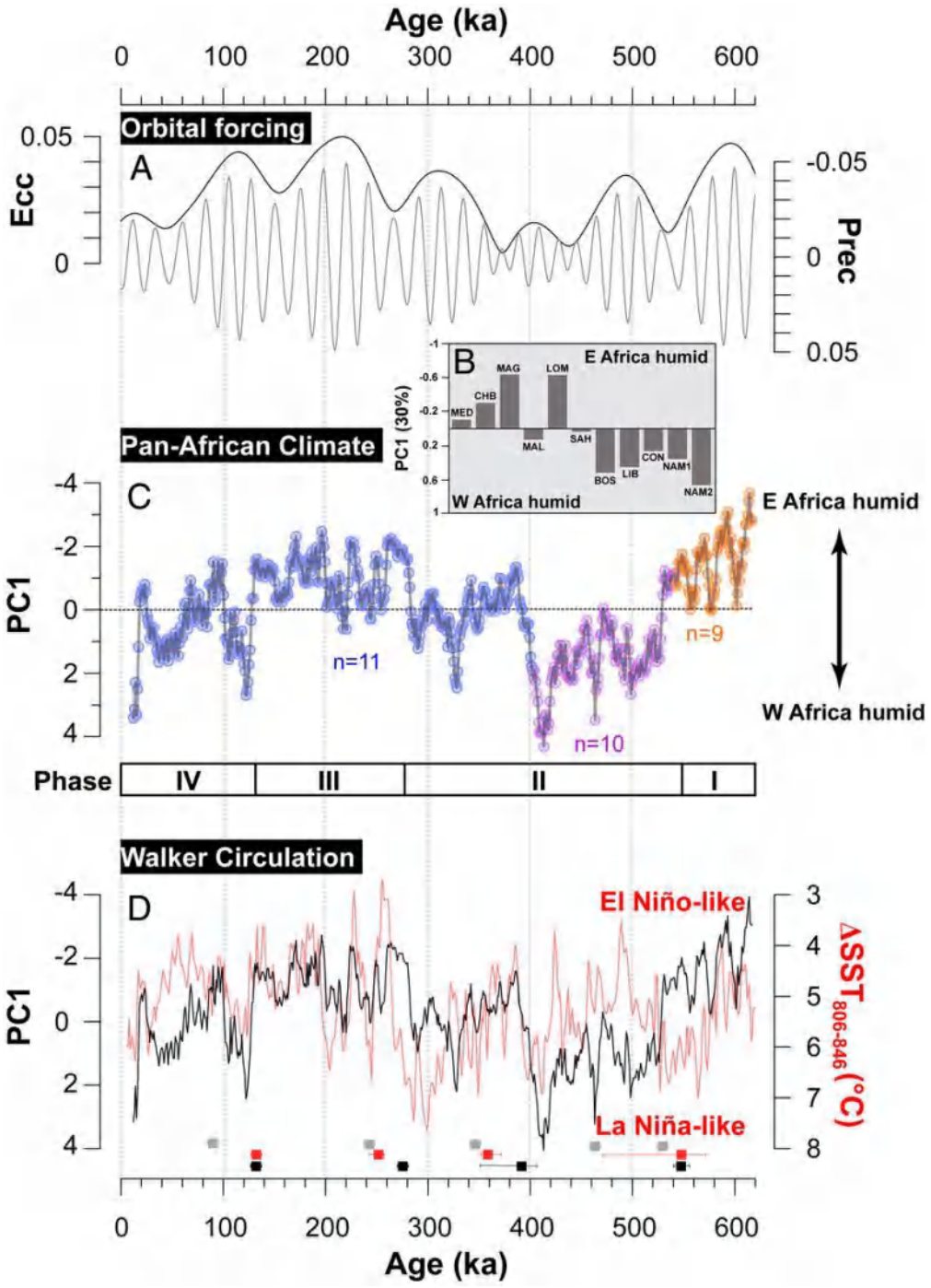

Figure 2. Pan-African climate variability during the last ~620 ky. (A) Orbital eccentricity (Left) and precession (Right) (59). (B) Average PC1 loadings derived from the pwPCA. (C) PC1 derived from the pwPCA. n = number of datasets used in each iteration. (D) Comparison between PC1 and the SST gradient (ΔSST; red line) between eastern Pacific Ocean Drilling Program (ODP) Site 806 (32) and western Pacific Ocean ODP Site 846 (33). Designation of El Niño– and La Niña–like conditions follows ref. 30. Breakpoints and their error bounds of PC1 (black boxes), ENSO (red boxes), and Earth´s eccentricity (gray boxes) are marked.

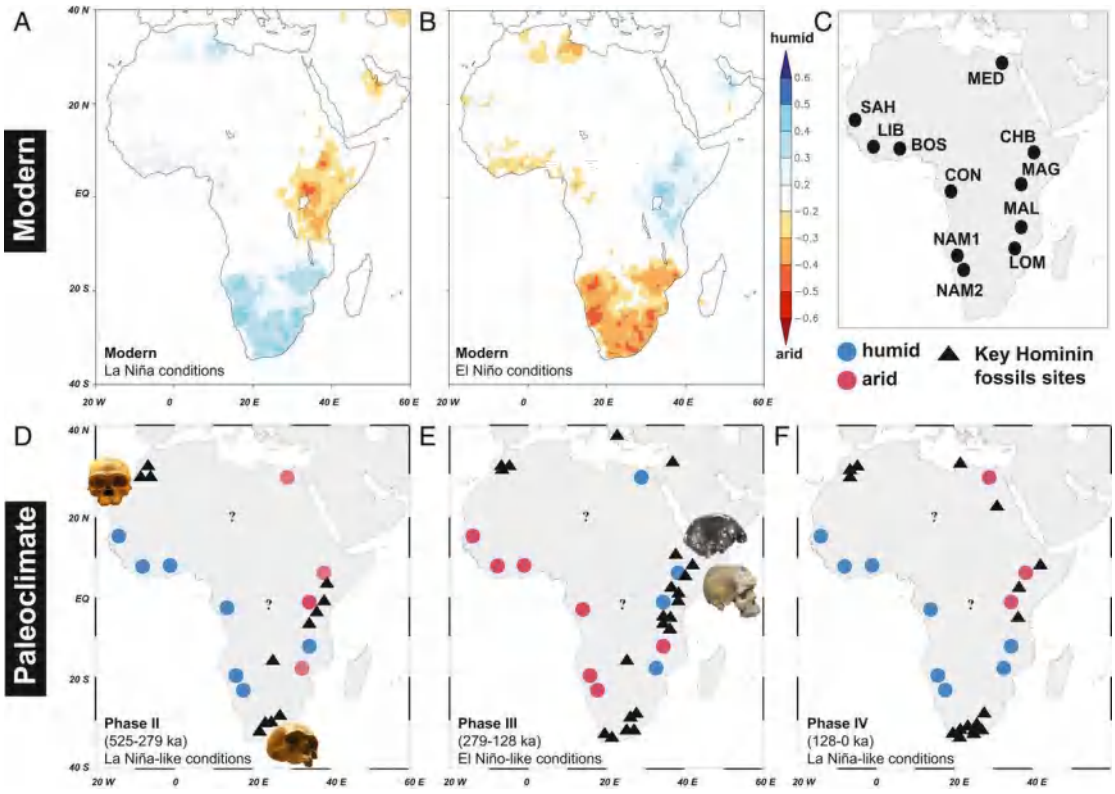

Figure 3. Pan-African climate variability relative to the fossil evidence for hominin evolution during the Middle and Late Pleistocene. A and B show the Spearman correlation coefficients for the months October to April from years 1891 to 2016 of the NINO3.4 index and the Global Precipitation Climatology Centre (V2018 land) precipitation data in a 0.5° grid. Positive correlation coefficients = humid conditions; negative correlation coefficients = arid conditions. The spatial correlation shown is significant with P > 10%. Analysis and visualization can be found at the following: https://climexp.knmi.nl/start.cgi. C displays the location of the study sites used for the reconstruction of pan-African climate variability. The full list of abbreviations, references, and coordinates for all sites is provided in SI Appendix, Table S1. D–F present the spatiotemporal distribution of moisture during Phases II, III, and IV, thus encompassing a full ~400-ky eccentricity cycle. The designation of humid/arid (blue/red) for each study site (circle) derives from the calculation of the proxy median for the respective time slice relative to the reference median value of the entire data population across the last ~620 ky (see Materials and Methods for details; SI Appendix, Table S3). The list of key hominin fossil sites traces are marked by black triangles (see SI Appendix, Table S4 for references). Photographs in D are from Ryan Somma/Wikimedia Commons. Photographs in E from the top, modified from ref. 60, are from Addis Ababa National Museum/Wikimedia Commons.

14. 地球磁场强度：中古生代偶极场低值的证据

翻译人：张伟杰 12031188@mail.sustech.edu.cn

Hawkins L M A, Grappone J M, Sprain C J, et al. ***Intensity of the Earth's magnetic field: evidence for a Mid-Paleozoic dipole low*** *[J]. Proceedings of the National Academy of Sciences, 2021, 118(34).*

https://doi.org/10.1073/pnas.2017342118

摘要：中生代偶极场低值阶段（MDL）持续了至少约 80 百万年，结束于白垩纪正极性超时起始的时间。最近对西伯利亚地区泥盆纪的研究发现，在二叠纪-石炭纪反极性超时（PCRS）之前的几千万年也有类似的低场阶段。为了限制这个潜在偶极场低值阶段的长度和时间，本研究提供了来自英国 Strathmore（约 411～416Ma）和 Kinghorn（约 332 Ma）熔岩流的古强度评估值。两个地点都进行过古地磁极（Q 值为 6 到 7）研究，并根据古方向、岩石磁学分析和显微镜对这些地点的古强度适用性进行了评估。利用热和微波古强度实验确定了来自 Strathmore 和 Kinghorn 地区分别为约 3～51 μT（6～98 ZAm^2）和 4～11 μT（9～27 ZAm^2）的采点平均古强度评估值。这些数据以及来自（更新的）古强度数据库（PINT15）中从 200 到 500 Ma 的所有数据，都使用定性古强度标准（Q_{PI}）进行了评估。从这项研究和其他研究中获得的可靠的（Q_{PI} ≥ 5）弱的古强度值表明，从 332 Ma 到 416 Ma 为一段低偶极矩时期（中值场强为 17 ZAm^2）。“中古生代偶极场低值阶段（MPDL）”与 MDL 有许多相似之处，包括在 PCRS 开始附近场强出现显着增加。MPDL 还提供了倒转频率和场强之间的反比关系以及与地幔对流相关的古地磁行为中可能的~200 My 周期的支持。

ABSTRACT: The Mesozoic Dipole Low (MDL) is a period, covering at least ~80 My, of low dipole moment that ended at the start of the Cretaceous Normal Superchron. Recent studies of Devonian age Siberian localities identified similarly low field values a few tens of million years prior to the Permo-Carboniferous Reverse Superchron (PCRS). To constrain the length and timing of this potential dipole low, this study presents paleointensity estimates from Strathmore (~411 to 416 Ma) and Kinghorn (~332 Ma) lava flows, United Kingdom. Both localities have been studied for paleomagnetic poles (Q values of 6 to 7), and the sites were assessed for their suitability for

paleointensity from paleodirections, rock magnetic analysis, and microscopy. Thermal and microwave experiments were used to determine site mean paleointensity estimates of ~3 to 51 μT (6 to 98 ZAm^2) and 4 to 11 μT (9 to 27 ZAm^2) from the Strathmore and Kinghorn localities, respectively. These, and all the sites from 200 to 500 Ma from the (updated) Paleointensity database (PINT15), were assessed using the Qualitative Paleointensity criteria (Q_{PI}). The procurement of reliable ($Q_{PI} \geqslant 5$) weak paleointensity estimates from this and other studies indicates a period of low dipole moment (median field strength of 17 ZAm^2) from 332 to 416 Ma. This "Mid-Paleozoic Dipole Low (MPDL)" bears a number of similarities to the MDL, including the substantial increase in field strength near the onset of the PCRS. The MPDL also adds support to the inverse relationship between reversal frequency and field strength and a possible ~200 My cycle in paleomagnetic behavior relating to mantle convection.

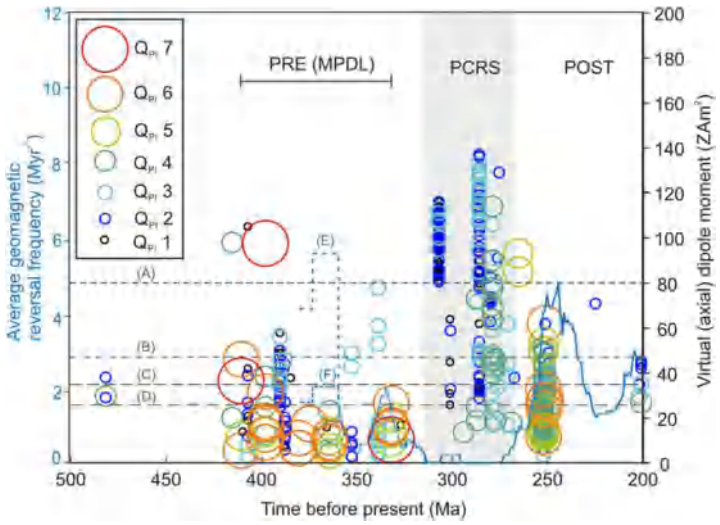

Figure 1. The age distribution of all the virtual (axial) dipole moment [V(A)DM] values with Q_{PI} >0 between 200 and 500 Ma. Summaries of the Q_{PI} scores applied to each of the studies from this period are outlined in Datasets S3 and S4. The size and the color of the circles representing the V(A)DM values corresponds to the Q_{PI} scoring as outlined in the key. The PRE, PCRS, and POST sections refer to the same age bins used for the Kolmogorov-Smirnov tests in Fig. 5 and SI Appendix, Table S2. The dashed lines represent (A) the present day field strength (50), (B) CNS at $Q_{PI} \geqslant 3$ (16), (C) JHAP $Q_{PI} \geqslant 3$ (16), (D) JHAP $Q_{PI} \geqslant 0$ (16), (E) the maximum possible, and (F) the minimum possible reversal frequency from the Canning basin magnetostratigraphy (45).

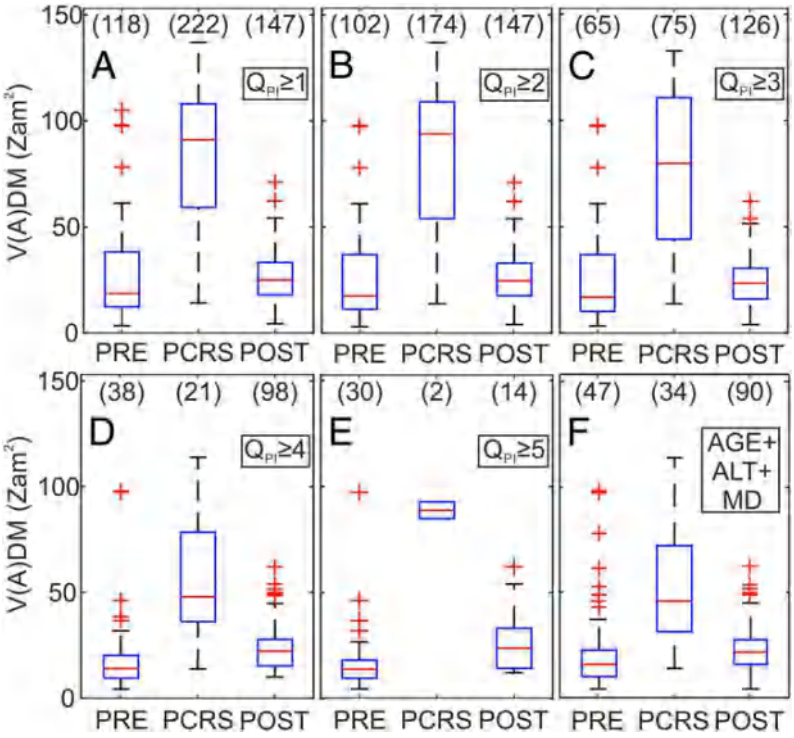

Figure 2. Boxplots showing the V(A)DM distribution of the PRE, PCRS and POST bins (same as in SI Appendix, Table S2). The boxplots are filtered based on the total QPI scores applied to the sites, between $Q_{PI} \geqslant 1$ and $Q_{PI} \geqslant 5$ (A – E) and for sites that pass the AGE, ALT, and MD criteria (*F*). The numbers over the boxes display the number of sites in each of the age bins. On each box, the central mark is the median, the edges of the box are the 25th and 75th percentiles, the dashed lines extend to the most extreme data points not considered outliers, and outliers are plotted individually (+).